Research Article
Geochemistry, Geophysics, Geosystems
DOI 10.1002/2013GC005198

Maar-diatreme geometry and deposits: subsurface blast experiments with variable explosion depth

Graettinger, A.H.[1]; Valentine, G.A.[1]; Sonder, I.[1]; Ross, P.-S.[2], White, J.D.L.[3], Taddeucci, J.[4]

1 Center for Geohazards Studies, 411 Cook Hall, University at Buffalo, Buffalo, NY, 14260, USA

2 Institut national de la recherche scientifique, centre Eau Terre Environnement, 490, Rue de la Couronne, Québec (QC), G1K 9A9, Canada

3 Geology Department, University of Otago, Dunedin, New Zealand

4 Istituto Nazionale di Geofisica e Vulcanologia (INGV), Roma, Italy

Received: Dec 10, 2013; Revised: Jan 29, 2014; Accepted: Feb 04, 2014

Abstract

Basaltic maar-diatreme volcanoes, which have craters cut into pre-eruption landscapes (maars) underlain by downward-tapering bodies of fragmental material commonly cut by hypabyssal intrusions (diatremes), are produced by multiple subsurface phreatomagmatic explosions. Although many maar-diatremes have been studied, the link between explosion dynamics and the resulting deposit architecture is still poorly understood. Scaled experiments employed multiple buried explosions of known energies and depths within layered aggregates in order to assess the effects of explosion depth, and the morphology and compaction of the host on the distribution of host materials in resulting ejecta, the development of sub-crater structures and deposits, and the relationships between them. Experimental craters were 1-2 m wide. Analysis of high-speed video shows that explosion jets had heights and shapes that were strongly influenced by scaled depth (physical depth scaled against explosion energy) and by the presence or absence of a crater. Jet properties in turn controlled the distribution of ejecta deposits outside the craters, and we infer that this is also reflected in the diverse range of deposit types at natural maars. Ejecta were dominated by material that originated above the explosion site, and the shallowest material was dispersed the farthest. Subcrater deposits illustrate progressive vertical mixing of host materials through successive explosions. We conclude that the progressive appearance of deeper-seated material stratigraphically upward in deposits of natural maars probably records the length and time scale for upward mixing through multiple explosions with ejection by shallow blasts, rather than progressive deepening of explosion sites in response to drawdown of aquifers.

Key points (less than 80 char)

- Blast experiments successfully recreate maar-diatreme like structures
- Ejecta distribution is controlled by scaled depth and ground condition

- Componentry indicates deeply sourced lithics are erupted by multiple blasts
- Only shallow blasts emplace ejecta to form extra-crater deposits

1.0 Introduction

Basaltic maar-diatreme volcanoes are the result of multiple subsurface explosions produced by the interaction of magma and groundwater. This results in a crater below the previous ground surface, with proximal ejecta forming a low tephra (ejecta) ring, plus distal fall and density current deposits that cover the surrounding landscape. Beneath the crater a diatreme structure extends downward in a funnel-like shape and terminates with an irregular root zone (Ross and White 2011 and references therein). Direct observations of historical maar-diatreme volcanoes are limited to a few examples, with the best descriptions from the 1977 Ukinrek Maars in Alaska (Kienle et al. 1980; Self et al. 1980). Detailed descriptions of surface (crater and tephra ring) or subsurface (diatreme) structures of pre-historic examples of these volcanoes are available from several locations (e.g., Hearn 1968; White 1991; Brand and Clarke 2009; Valentine et al. 2011; Ross et al. 2011; White and Ross 2011; Lefebvre et al. 2013), however, there is only one, small example where the eruptive deposits, landform, and the subsurface diatreme are all preserved and exposed (Geshi et al 2011). Certainly there are no examples where direct observations of eruption dynamics can be combined with integrated field data of a maar and its diatreme.

Investigations of these volcanoes have helped evolve a model of maar-diatreme formation, where subsurface explosions occur at multiple depths and lateral locations, and there is increasing evidence that only shallow explosions produce extra-crater deposits (White and Ross 2011; Valentine 2012; Valentine and White 2012). Additionally, crater growth is known to be from a combination of explosive and collapse processes (Hearn 1968; Houser 1969; Ross et al. 2011). Many questions about the relationships between explosion dynamics and the resulting geological features can only be addressed experimentally; we focus on three sets of questions in this paper. First, how do explosion energy, depth, and number control maar-diatreme size and shape? Second, how are lithics that originate at different depths beneath a volcano distributed onto the surface as a function of explosion energy, depth and number of explosions? Finally, how do explosion processes control the formation of diatremes, and what is the relationship between diatreme deposits and erupted deposits? Here we use outdoor, meter-scale, experiments that simulate subterranean phreatomagmatic explosions in layered media (referred to as pads) to investigate the deposits and structures produced above and below the surface. The integration of video observations of depositional processes, "before" and "after" morphological data, and granulometry and componentry of samples is unique to this experimental setup. The experiments are essentially small-scale eruptions, but are sufficiently large to scale well with natural eruptions, and are studied by the same geological and monitoring techniques that would ideally be used at a real volcano. Unlike natural eruptions, the experiments are conducted with excellent control on initial and boundary conditions (Valentine et al. 2012; Ross et al., 2013; Taddeucci et al., 2013).

The experiments show that explosion depth, explosion energy, and a combination of pad conditioning and surface topography all contribute to the size and shape of the resulting jet and consequently surface expression (crater and distribution of ejecta). Extra-crater deposits (ejecta) reveal that material escapes the crater with shallow blasts. Consequently, lithics found within proximal deposits are not directly reflective of the depth of explosion that produced those same deposits. Multiple subsurface explosions near or below an optimal depth of burial, produce complex sub-vertical domainal and subsidence structures in the subsurface, resembling diatremes. Deposits that form below the craters (subcrater) are the result of both upward (explosion-driven) and downward (subsidence) mixing, and produce two major facies.

2.0 Methods and definitions

The experiments were conducted using buried chemical explosives (PENTEX booster charges) of 0.15 to 0.45 kg, with energy density estimated to be ~5 × 10^6 J/kg. The depth of burial and charge energy were varied in five experiments conducted in compacted, layered aggregate. The setup is intended to mimic discrete subsurface volcanic explosions in a layered substrate. Natural phreatomagmatic interactions are known to produce discrete blasts, and studied phreatomagmatic explosions (molten fuel-coolant interactions, MFCI; Büttner and Zimanowski, 1998) are very rapid. The detonation wave speed associated with the chemical explosives used in these experiments is, however, even faster than is expected in an MFCI (Büttner and Zimanowski, 1998) and the initial coupling of explosion energy to the surroundings might differ. Nevertheless, for the purposes of this investigation, which focuses on large-scale phenomenology and resulting landforms and deposits, the analogy between chemical and MFCI explosions is reasonable. The experiments are designed to investigate the relationship between the location of a subsurface explosion at various energies and the resulting deposits, which can be discussed in terms of scaled depth:

$$D = \mathrm{d}/\mathrm{E}^{(1/3)} ,$$

where d = depth of charge burial (depth of material immediately above the charge) and E is energy of the explosion in joules with scaled depth units expressed as $\mathrm{m/J}^{1/3}$.

2.1 Blast set-up

The blasts were executed in two trenches filled with 15 cm-thick layers, in order from bottom to top: red gravel (A), pea gravel (B), concrete sand (C), recycled asphalt (D), poorly sorted limestone sand (E)(Fig. 1; Supplementary Table 1). One trench, which hosted three experiments, was shallow (75 cm) and contained layers B-E. A second, deeper trench was filled with layers A-E and hosted two experiments. A 15-30 cm thick layer of mixed aggregate and soil underlay layer A in both trenches. Each layer was compacted and the final thicknesses were confirmed to be within +/- 1 cm of the intended 15 cm. The surface of the layered system was covered with a 1 cm-thick layer of white aragonite gravel (coarse sand and granules, Layer F) to serve as a marker of the flat pre-blast surface. Each experiment was conducted in a 3 m × 3 m 'pad' in one of the trenches where between one and three explosions were executed, for a total of 12 blasts (Table 1). Each of the five pads also had four ~7.5 cm diameter vertical holes filled with the white aragonite with a spacing of 25 cm radially away from the explosion epicenters, to serve as markers of subsurface deformation. The hole for each charge was created using a 10 cm diameter pipe that was hammered into the pad. The contents of the pipe were removed to enable precise charge placement with minimal disruption of the artificial strata. The placement of the charge occurred just before detonation, with a delay of up to one hour between the execution of each blast. Every charge hole was filled with brown-colored aquarium gravel after the placement of the charge and pressed by hand, not compacted.

Pad 1 had a single 0.45 kg charge buried at its optimal depth for crater excavation (Goto et al., 2001). Pad 2 had two consecutive and co-located, 0.3 kg charges at the same depth as Pad 1. Pad 3 had three blasts of 0.15 kg each with a different depth of burial that maintained at least 50 cm of immediate overburden. Pads 4 and 5, in the deeper trench, focused on deep blasts (1 m) with 0.15 kg charges. Pad 4 had a constant charge position, while Pad 5 had a charge position that moved progressively toward the surface. For simplicity, each blast will be referred to by an abbreviated code of pad number followed by blast number (e.g. P1B1 for Pad 1 Blast 1).

2.2 Blast observations

The blasts were recorded using a variety of equipment including seismic, acoustic, and electrical field sensors. Here we focus on high speed (300 fps, 512 x 384 resolution) and high definition (30 fps, 1920 x 1080 resolution) video that shows the evolution of the blast jets from onset to deposition. Additional video and geophysical data will be discussed in other publications. The evolution of jet shapes is described, and important features quantified: maximum jet height, maximum jet width (top and bottom of jet), the time to the onset of deposition, and the time to the completion of deposition. The onset of deposition was determined to be the first significant downward motion of material near the pad surface, and the completion corresponded to the cessation of motion of coarse material. A dilute dust cloud lingered in the air over the explosion sites, but did not produce sufficient deposits to sample, so its timing was not calculated.

Jet shape is described as a ratio of the width of the top of the jet relative to the base (Wt/Wb), where the base width is the greatest width of the jet at or just above the pad surface, and top width is defined as the widest diameter of the curve that defines the top of the dense jet (Fig. 2). Wt/Wb characterizes the motion of the debris within the jet at its maximum extent relative to horizontal start position and is independent of height, which was measured separately. This property is comparable to ‘jet angle’, a measure of the angle between the sides of the jet, used in Taddeucci et al. (2013).

2.3 Measurements, excavation and sampling

Following each blast the pad and surrounding area were documented using still photography. The features produced by each blast include either a broad crater, a pile of material in a depression (referred to as a retarc; Houser 1969), or a narrow steep-sided subsidence pit. The final feature of each experimental pad was either a crater or a subsidence pit. Visual observations were recorded in conjunction with orthogonal topographic profiles of the surface structures measured at 10 cm intervals. For most blasts a penetrometer ("soil compaction tester" modified to have a flat circular tip 1 cm in diameter) and/or a metal rod (1.6x 1.0 cm in section, rectangular shape) was inserted into the subsurface to the point of increased resistance (compaction profiles); this provides a semi-quantitative measure of the extent of subsurface disruption of the layered aggregates. Blasts typically decrease the compaction of the aggregate near the charge position, so when possible (Pad 4 and 5) compaction profiles were collected between each blast to monitor the progressive changes in compaction resulting from multiple blasts. The metal rod was used in cases where the length of the penetrometer was insufficient to reach the depth of compaction. Here we use the term 'subcrater' for all structures and deposits beneath the crater floor; this is not a genetic term implying transport mechanisms.

Ejecta is defined here as material thrown from the explosion site and deposited outside the craters (see also Ross et al., 2013). Ejecta samples were collected in 0.25 m^2 trays arranged in two radial arrays starting 2 m from each blast epicenter and extending outward to 17 m (Fig. 1). Box spacing was 1 m (center to center). One additional sample container was placed 1.5 m from the blast epicenter. Ejecta distribution is described in terms of crater radius as in Lee and Mazzola (1989) and Gould (1981). Here we divide ejecta into 1) Proximal ejecta, the topographically high area immediately surrounding the crater rim, where the deposits reach their maximum thickness; 2) Medial ejecta is a thin but continuous sheet and is here characterized in terms of mass per unit area (> 0.1 kg/m^2); and 3) Distal ejecta consists of isolated clasts beyond the medial blanket. The proximal-medial and medial-distal boundaries are somewhat subjective and in reality are gradational. Componentry of the samples was analyzed to determine the weight percentage of the different material types in each sample.

A ditch was dug along the outer edge of the two experimental trenches after the blasts were complete. This provided access for cross-sectional examination of the subsurface features created by the experiments. Each pad was then excavated incrementally with reference photos and detailed descriptions of vertical faces produced every ca. 20 cm. Samples were collected from deposits within the crater rim, crater bottom, and subcrater deposits. Subsurface and ejecta samples were analyzed for componentry. Reference photographs were used to make measurements of angles and the size of structures in the subsurface to supplement observations made in the field.

3.0 Results: experiments by Pad

3.1 Pad 1

Pad 1 had one blast at approximately the optimal depth of burial for maximum crater excavation, defined by a scaled depth of 0.0035 m/$J^{1/3}$ (Table 1; Goto et al. 2001). At this scale 0.45 kg was buried under 50 cm of aggregate (same as Pad 1 from previous experiments; Valentine et al. 2012). This pad serves as a control to investigate the simple blast system using updated monitoring processes and complex set up (thinner layers and more instrumentation) and as a link to the 2012 experiments. It also represents the simplest scenario for comparison with subsequent, more complicated pad experiments.

3.1.1 Pad 1 Jet phenomenology, crater morphology and ejecta

The blast initially produced a rounded dome that expanded to form discrete fingers having high particle concentration (Video 1). Deposition began at the base of the jet while expansion continued at the top, forming an upside-down trapezoid shaped jet (Fig. 2). Most material was deposited within a few meters of the blast center from direct collapse at the base of the jet, and then deposition moved progressively outward as jet fingers collapsed. Isolated ejecta clasts traveled farther and deposition of coarse material took roughly 3 seconds. A dilute cloud of dust hovered over the site, but did not leave detectable deposits. The single blast at Pad 1 produced a well-defined crater nearly 2 m in diameter, with an undulating rim and a surrounding subtle second ring (Fig. 3). Beyond the second rim the deposits were distinctly rayed in map view. Rays traced back toward the crater rim where they formed distinct ridges extending outward from highs along the rim. The distribution of rays was irregular, but typically on the order of 10-20 cm apart at the crater rim.

Ejecta deposition (Fig. 4) decreased rapidly with distance (4 $\text{kg}\cdot\text{m}^{-2}$/m) out to ~5 m from the epicenter, followed by a more gradual decrease representing deposition of scattered particles (distal ejecta). This trend was seen in previous experimental results (Valentine et al. 2012). Ejecta travelled up to 16 m from the blast center and was composed of materials from the top four pad layers (overwhelmingly layers D and E, i.e. the top 30 cm of the pre-blast stratigraphy, plus the ground marker layer F), plus aquarium gravel from the charge hole (Fig. 5). The greatest depth of excavation as inferred from ejecta componentry was 0.45 m, just 5 cm above the emplaced charge (0.5 m below the pad surface). Ejecta were enriched in layer D clasts near the crater, but D clasts were progressively replaced by layer E and layer F clasts (derived from shallower depths in the pad) with increasing distance. Up to 5% of layer B material (in which the charge was placed) was detected in the proximal ejecta. Minor amounts (ca. 1.5 wt. %) of layer B were collected in the medial ejecta. Black chemical precipitate was common on clasts in the distal ejecta.

3.1.2 Pad 1 Subsurface structure and deposits

Excavation of Pad 1 revealed deposits in the immediate subcrater that displayed weakly developed bedding following the curved inner wall of the crater (Fig. 6 and 7). The components of the deposits were mixed, with local centimeter to decimeter scale domains dominated by individual material types. We use the term ‘domain’ to describe a body having relatively consistent internal composition within a deposit, but which is not a bed or layer. These layered deposits had sharp basal contacts. Below the bedded subcrater deposits were deposits comprising vertically concentric domains in which unmixed deeper layer C occurred at the center of the structure. The margins of the domainal subcrater structure were defined by a lateral transition from preexisting layers into deformed, inward dipping layers that extended into steeply angled domains within the concentric structure. Material from layer B was not present in the vertical domains, but instead had a synformal structure below the crater. The compaction profile reached a depth of 0.80 m below the original pad level (Table 2). Laterally the profile (slope of 68°) corresponded with the transition from undeformed host layers to downward-deformed layers. Beyond the crater rim, the original layers show an apparent outward dip. This phenomenon was also reported by Ross et al. (2013) for a comparable experiment.

In the following we continue to describe subcrater deposits as either bedded or domainal. Bedded deposits contain layers that are parallel or subparallel to the bounding surfaces of the facies (the base of the bedded deposits approximately parallels the bowl-shaped crater floor).

Domainal deposits contain irregularly shaped domains of different compositions that can have steep to near vertical contacts.

3.2 Pad 2

Pad 2 had two co-located blasts (Table 1) to investigate the relationship between scaled depth and a disrupted pad that included a crater, with a focus on the ejection process. The first explosion occurred near the optimum depth of burial. The second blast occurred in a disturbed pad under an existing crater, and the immediate overburden was about 27 cm for P2B2, which was less than the optimal depth of burial (2.03×10^{-3} m/J$^{1/3}$). The total explosive energy used in Pad 2 was 1/3 greater than that used for Pad 1.

3.2.1 Pad 2 Blast 1 Jet phenomenology, crater morphology and ejecta

The first blast at Pad 2 produced a broad initial jet with a visible black gas cloud from the explosive. The ejecta moved upward as a jet comprising numerous individual fingers that was wider at the top than the base (Fig. 2). Deposition began from the base of the jet, while minor expansion occurred at the top, so that some (medial) ejecta reached the sample boxes before upward jet growth ended. A dust cloud lingered above the pad after the main jet collapsed. The blast produced a 1.5 m diameter, 0.3 m deep crater with a sharp ragged edge, which was surrounded by a subtle second rim with a height of only a few cm (Fig. 3). The ejecta had a noticeable rayed distribution, but the associated undulations in the crater rim were subtle. The rim was prone to collapse.

Although the total mass of ejecta collected was less than P1B1, the mass of ejecta per unit area decayed with increasing distance at a similar rate as for P1B1 (Fig. 4). Distal ejecta travelled up to 15 m from the blast site (Table 1). Ejecta from this blast was dominated by material from layer E with lesser amounts of clasts from layer F, layer D, and aquarium gravel (Fig. 5). Material from layer F is dominant further away from the crater, as it was for P1B1. The greatest depth from which ejecta originated was 0.3 m; the charge was placed at 0.5 m. Debris from layer D, which forms a good proportion of overall ejecta for P1B1, is nearly absent in the P2B1 ejecta, although the charges were detonated at the same depth as the previous blast. Black chemical precipitate was common on clasts in the distal ejecta.

3.2.2 Pad 2 Blast 2 Jet phenomenology, crater morphology and ejecta

The jet initiated as a cloud of black gas followed by a mass of debris that rapidly developed into an expanding jet with individual fingers at its top (Fig. 2). As the jet base expanded the P2B1 crater rim was displaced outward (Video 2). Deposition began at the base, while a dilute dusty cloud continued to rise. P2B2 increased the crater diameter and produced the deepest crater and greatest depth to diameter ratio in these experiments (Table 1, Fig. 2). Thinly bedded proximal ejecta were exposed on the steep inner side of the crater rim, and there were well-defined slumped masses in the bottom of the crater below. Large clumps of layer E material were common in the crater bottom with clasts of layer D in a matrix of layer E material.

Medial ejecta for this blast only reached 4 m from the blast center, but distal ejecta traveled as far as 18 m from the blast epicenter, the furthest of any blast within these experiments. P2B2 ejecta were dominated by layer D clasts, with lesser amounts from layer E and of aquarium gravel (Fig. 5). The layer D ejecta originated ~0.2 m above the charge position (Fig. 8). Black chemical precipitate was common on clasts in the distal P2B2 ejecta.

3.2.3 Pad 2 Subsurface structure and deposits

The Pad 2 crater was lined with weakly bedded subcrater deposits of mixed material from layers C-E (Fig. 6). The crater extended down into layer C, where the bedded subcrater deposits had an irregular contact with the underlying domainal subcrater deposits. Local domains of layer D material extended upward, like a folded flap, into the overlying bedded subcrater deposits. Immediately below the crater, layer C dipped downward and layer B displayed significant thinning to ~5 cm thickness. The disruption profile extended to a depth of 1.0 m, and profile edges coincided with the transition between the host material and the deformed, downwarped, domainal subcrater deposits (Fig. 7). The average profile-edge angle was 50°, significantly less than for the previous pad.

3.3 Pad 3

This pad built on the experience of the 2012 experiments (Valentine et al. 2012), using three charges in sequence where the scaled depth remained constant, and thus the total depth below the original pad surface increased. It tested the Lorenz type maar-diatreme model (Lorenz 1986), and investigated the relationship between explosion depth and the excavation of the host material as recorded in ballistic deposits (Table 1). All explosions were buried deeper than the optimum depths for the 0.15 kg charges.

3.3.1 Pad 3 Blast 1 Jet phenomenology, crater morphology and ejecta

The blast initially produced a uniform dome that expanded to form discrete fingers. A distinct core of aquarium gravel travelled ahead of the rest of the jet (Fig. 8). Deposition began when lateral expansion of the base stopped. Fines began to loft from the base of the jet as deposition of coarser material continued. As the jet thinned due to deposition, a 26 cm-high retarc became visible on the pad surface. The retarc appeared to be composed of layer D with a coating of aquarium gravel within a subtle 1.8 m diameter, 2-3 cm deep circular depression (Fig. 3). Discrete rays of ejecta (layer E) surrounded the rim of the depression with a spacing of tens of centimeters.

This blast produced minor medial and distal ejecta. The material in the retarc did not leave the depression and therefore is not considered ejecta. Medial ejecta extended 3 m from the blast site with the same geometric spreading ($1/r^2$ decay) dominated distribution as observed in P1B1 and P2B1 (Fig. 4). Distal ejecta reached only 4 m from the blast site. The ejecta contained material from the surface layers E and F and trace amounts of layer D (< 1 wt. %; Fig. 9). The charge originated 0.5 m below the pad but ejected material mostly from depths less than 0.15 m.

3.3.2 Pad 3 Blast 2 Jet phenomenology, crater morphology and ejecta

The blast produced initial deformation of the P3B1 retarc from its base, and then the whole mass rose as material jetted from the slopes of the retarc. The jet shape was dominated by outward expansion (Fig. 8; Video 3). After the deposition of coarser clasts, a ground-hugging cloud of fines lingered at the site before dissipating. P3B2 produced a more typical crater, but with a smaller diameter than that of the depression caused by the first blast (Fig. 3). The crater had a subtly undulating rim. The inside surface of the crater was dominated by larger clasts from layer D.

Blast 2 produced proximal (up to 14 cm thick) and minor medial ejecta. The mass of material collected from the second blast was less than the first, but medial ejecta extended to 4 m beyond the blast epicenter. Distal ejecta was minor, but was collected up to 5 m from the blast site. Ejecta from Blast 2 was dominated by material from layer D with < 10 wt. % of material from layers E and F (Fig. 9). The blast occurred at 0.4 m below the original pad surface, and material was ejected from < 0.3 m (base of layer D).

3.3.3 Pad 3 Blast 3 Jet phenomenology, crater morphology and ejecta

The whole pad area deformed before a jet rose from the center of the previous crater. As deposition began at the base of the crater, dusty gas escaped laterally as it was expelled from the collapsing, coarser-grained mixture that collapsed back into the crater (Fig. 8). The final crater was slightly larger in diameter, but smaller depth to diameter ratio, than the previous blast (Table 1; Fig. 3). The crater walls had steep 1-3 cm high edges along the rim.

This blast produced limited ejecta so that rays of deposits from P3B1 blast were still discernible on the pad surface. Medial ejecta extended only 2 m from the center, with distal ejecta reaching 4 m from the blast center. The componentry of these ejecta was diverse, with a preponderance of layer D clasts and aquarium gravel (Fig. 9). The remaining ejecta comprised small amounts of layer C, layer E and layer F clasts. While this charge was placed at 0.74 m, material was ejected only from a depth of < 0.45 m (base of layer C). Proximal ejecta for P3B3 consisted predominantly of mixed layer E and layer F clasts.

3.3.4 Pad 3 Subsurface structure and deposits

The subsurface structure produced by the three blasts included well-developed bedded subcrater deposits to a depth of 0.4 m below the original pad surface and domainal subcrater deposits to a depth of 0.75 m (Fig. 6). The compaction profile showed disruption 1 m below the pad surface, which was 0.26 m below the deepest charge in the experiment. The bedded subcrater deposits included discontinuous, centimeter-thick lenticular beds parallel to the crater floor and contained clasts from all of the layers forming this pad (B-E) except for the surface layer F, which was completely removed from the crater area. Interbedded with the mixed materials were beds of unmixed materials from layers B-E. The domainal subcrater deposits included vertically concentric domains of material from layers B, C and D. Layer E was disrupted within the diameter the crater, but was not as greatly deformed as the lower units (Fig. 6). The contacts between units in the subcrater deposits were irregular, with complicated folds along near-vertical boundaries. Outside of the disrupted zone, layer C contained downward propagating tension cracks filled with material from overlying layer D. The disruption profile was broad near the surface and steep at the center, with an average slope of 39°.

3.4 Pad 4

Pad 4 and 5 focused on deeply buried charges. All charges in Pad 4 were detonated at the same depth of 1 m below the original pad surface to investigate the potential for mixing in the subsurface with repeated, co-located explosions such as might occur at a stationary water table or other fixed volcanic explosion site in a natural maar-diatreme (Table 1).

3.4.1 Pad 4 Blast 1 Jet phenomenology, crater morphology and ejecta

This blast produced upward doming of the whole pad surface followed by the growth of a very small (~30 cm high) jet (Fig. 8). The jet fell back to the pad surface without significant alteration to the surrounding pad. No gas venting or fines escape was observed (Video 4). A small central area subsided after deposition had ceased to form a small pit (we use the term ‘pit’ to distinguish depressions formed dominantly by subsidence from craters, formed mainly by explosive excavation). No ejecta escaped the central pit. A series of subtle, concentric surface undulations could be seen in the distribution of aragonite on the pad surface (Fig. 3).

3.4.2 Pad 4 Blast 2 Jet phenomenology, crater morphology and ejecta

This blast produced a short central jet shaped like a stretched dome (Fig. 8). The jet collapsed back into the pit, expelling a fine-grained density current that flowed radially outward. Ring fractures formed around the crater as deposition was complete. All material was deposited in the pit (no ejecta was collected). A shallow (12 cm deep from the rim) circular subsidence pit 80 cm across was formed, nearly twice the diameter of the previous pit, ringed by open concentric fractures (Fig. 3). The circular pit was located within a gently domed area ca. 5 cm high relative to the original surface of the pad. The pit floor was noticeably disrupted, unlike in the first blast, revealing material from layer E.

3.4.3 Pad 4 Blast 3 Jet phenomenology, crater morphology and ejecta

This third blast caused the ground surface to rise and initially closed the fractures produced by the previous blast. A small dome-shaped jet formed with a diameter constrained by the crater (Fig. 8). A cloud of fines hovered over the jet, and then both the coarse and fine material collapsed back into the pit (no ejecta was collected). P4B3 produced a pit slightly larger than Blast 2 (Table 1), but the margins were subtle and domed, rather than fractured (Fig. 3). The floor of the pit was more homogenous in color as the two surface units (E, F) were mixed.

3.4.4 Pad 4 Subsurface structure and deposits

Excavation revealed a deep subcrater structure that consisted of centrally downwarped pad layers. No bedded subcrater deposits were observed, but there was minor disruption and mixing of material from layer F and E in the upper centimeter of the crater floor. The downwarped layers had variable thicknesses, but vertically bounded domains were absent (Fig. 6 and 7). At the center of the structure layer B increased in thickness by 10 cm. Layer A was approximately 20 cm thick at the center of the structure, but thinned dramatically to a few centimeters towards the side of the structure. The disrupted zone, determined by penetrometer, corresponded with the final depth of layer A, which was 20 cm below the depth of charge placement. Disruption profiles were collected after every blast and revealed a widening of the disturbed zone, and progressive shallowing of the angle of the disruption boundary from 72°, to 63° and finally 51° by the final blast (Fig. 8, Table 2). Clasts within the central zone of the structure were coated with a black chemical precipitate (Fig. 6). Samples of the subcrater structure immediately below the crater and near the depth of charge burial reveal minor mixing of material from layer D into layer E as well as layer A into layer B.

3.5 Pad 5

The final pad was used to investigate the influence of upward migrating blasts on mixing in the subsurface (Table 1). This progressive decrease in the scaled depth (and consequently depth below pad surface) was hypothesized to produce more complete mixing in the subsurface (Ross and White 2006; White and Ross 2011).

3.5.1 Pad 5 Blast 1 Jet phenomenology, crater morphology and ejecta

The first blast at Pad 5, with the same conditions as P4B1, produced an upward doming of the pad with a 0.3 m high jet, centered over the charge position (Fig. 8). The jet collapsed back to the pad without significant disruption of the surface material. P5B1 produced a minor central subsidence depression (Fig. 3). The collapse was uneven, with steep-sided fractures on one side, and slopes on the others. No ejecta were produced by this blast.

3.5.2 Pad 5 Blast 2 Jet phenomenology, crater morphology and ejecta

The blast resulted in broad uplift of the pad followed by a wave of fines that escaped from fractures on the edge of the P5B1 pit. A 0.7 m high, dome-shaped jet was produced within the limits of the pit and collapsed back into it (Fig. 8) with limited alteration of the pad surface. P5B2 produced a low angle retarc 8 cm in height within a well-defined subsidence pit (Fig. 3). The margins of the depression had minor open fractures between the crater and rim. No material escaped the pit.

3.5.3 Pad 5 Blast 3 Jet phenomenology, crater morphology and ejecta

Gas and fines escaped from the retarc before surface deformation began, and then the retarc expanded outward to form a jet that was constrained by the shape of the P5B2 pit, but expanded outward, low to the ground (Fig. 8). A low cloud of fines appeared as the coarse ejecta were deposited, and then dissipated slowly. P5B3 produced a shallow crater with a minor medial ejecta apron (Fig. 3). The surface of the apron was covered by layer D and a sub-linear deposit of aquarium gravel. The distal edges of the deposits displayed narrowly spaced, irregular rays. The inside of the crater had several concentric steps moving downward toward its center. The only blast of the deep series experiments to produce ejecta, P5B3 ejected the smallest total mass of any blasts. The ejecta contained only materials from the upper 15 cm of the pad (layer E and F clasts).

3.5.4 Pad 5 Subsurface structure and deposits

Excavation of Pad 5 revealed poorly-developed bedded subcrater deposits and a well-developed domainal subcrater deposit. The bedded subcrater deposits were thin (5-10 cm), weakly bedded, and consisted of layer E and D materials with abundant aquarium gravel (5 wt. %). The bedded subcrater deposits graded laterally into the mixed proximal ejecta of the crater rim. The domainal subcrater deposits share some similarities to the Pad 4 deposits, but had much greater variability along unit contacts. The near surface layers D and E had undulatory contacts that dipped downward at the center of the structure. Layer C had some minor undulations on its upper contact with layer D, but a more continuous contact with layer B. Notably, while layer C dips downward, the very center of the structure had local upward injection of layer B into layer C (Fig. 6). Similarly layer A intrudes into layer B on the scale of a few centimeters. Layer B displayed significant over-thickening at the center of the structure and extended more than 20 cm below its original base. Layer A was thinner at center of the structure, but deformed around the protruding layer B, and extended roughly 15 cm below its original layer boundary. The disruption profile (Fig. 8) became shallower and broader with each progressive blast, and its slopes decreased (85°-50°). The base of the final disruption profile was higher in the sequence than the base of the domainal subcrater deposits (Table 2, Fig. 6). Chemical precipitate was concentrated at the center of the structure, and extended into the mixed aggregate below layer A materials. Componentry reveals significant mixing in the lower portion of the domainal subcrater deposits where distinct domains of materials from above and below the main layer are present at the center of the structure. Beyond the rim of the final crater, most pad layers dip outward.

4.0 Integrated interpretation of processes and products

4.1 Effects of explosion energy, depth, and topography on ejecta distribution

Experiment videos reveal diverse jet shapes for the 12 blasts (Fig. 2 & 8), with significant similarities to jets of previous subsurface blast experiments (Ohba et al. 2002; Taddeucci et al. 2013). Maximum jet height, duration of deposition, and maximum ejecta distance are, to first order, inversely related to scaled depth in these experiments and those reported in Valentine et al. (2012), Ross et al. (2013) and Taddeucci et al. (2013) (Fig. 10; Table 1). Blasts at Pads 4 and 5, at scaled depths > 0.008 m/J$^{1/3}$, approximately twice the optimal depth of burial, produced minor jets (< 1.0 m high) with no ejecta. Ejecta were produced at Pad 5 only when the scaled depth had decreased to the level of the shallow blast experiments (Table 1). The lack of substantial venting at Pads 4 and 5 also resulted in considerable deposition of black chemical precipitates from the explosive in the subsurface.

For blasts that produced ejecta, deposit distribution was controlled by jet shape, with Wt/Wb > 0.5 required for deposition of ejecta beyond the crater (Fig. 11 and Table 1), and the distances reached by medial and distal ejecta are approximately proportional to Wt/Wb above this value. This trend is also reflected in the mass per unit area of ejecta (Fig. 4). The two main factors that affect Wt/Wb are the scaled depth and the presence or absence of a pre-existing crater or retarc (see Ohba et al. 2002, and Taddeucci et al. 2013). Both medial and distal ejecta increase in extent with decreasing scaled depth, until the optimal scaled depth of 0.004 m/J$^{1/3}$ is reached; this corresponds to optimal crater excavation (this study and Bening and Kurtz 1967).

For depths shallower than this optimal value, the trends of medial vs. distal ejecta diverge. As scaled depth decreases, the jet produced has a larger Wt/Wb and therefore distributes isolated distal ejecta widely (Ohba et al. 2002). In contrast, the extent of medial ejecta decreases markedly with jet height as more energy from the blasts is lost to the atmosphere (Fig. 10c).

Topography and pre-conditioning (disruption of the pad surface) also influenced jet shape and deposition patterns. In multiple blast experiments, jets through crater-free surfaces produced more extensive medial ejecta blankets than did those exiting through disrupted ground with topography. When jets erupted through a blast crater (e.g., P2B2), the ejecta deposit thinned more abruptly and the maximum extent of the medial ejecta decreased, because the initial expansion was vertically focused by the crater and more material simply fell or collapsed back into the craters instead of forming ejecta (Taddeucci et al. 2013). On the other hand, when the jet erupted from beneath positive topography (a retarc, i.e. Pad 3), the ejecta thinned less rapidly away from the crater because the jet had an important low-angle component as it erupted through the outer (lower) edges of the retarc. There was little high-angle ballistic ejection. For blasts that originate in disrupted ground, a jet erupted through a crater is vertically focused, while one erupted through a retarc is laterally focused (Fig. 12).

In contrast with medial ejecta distribution, the maximum distance of distal ejecta (isolated clasts) is not strongly affected by the presence of a crater (Fig. 10c) and instead correlates only with decreasing scaled depth. This dispersal of individual clasts beyond the more continuous medial ejecta is characteristic of deposits from discrete blasts, in contrast to those from continuous eruptions with a sustained plume (Self et al. 1980; Gould et al. 1981; Büchel and Lorenz 1993). We note that in natural eruptions, which have more fine-grained material in the erupted mixture, even jets that collapse back into the crater might expel a dusty gas that becomes a pyroclastic density current and move across an ejecta ring (see Valentine et al. 2012).

The experimental jets had particle-rich fingers, reflecting varying degrees of gas-particle coupling. For jets where the width of the top of the jet exceeds that of the width of the base (Wt/Wb > 1), these fingers follow ballistic paths at a range of angles and deposit material in rays that extend outward from the crater rims. Each finger begins deposition at or near the crater rim and then sediments progressively outward (Fig. 12), in the same manner that has been documented for ejecta deposition from impact craters (Melosh 1989). In some cases, fingers of poorly sorted material produce upon landing small, fine-grained density currents that extend outward from the finger's depositional axis. These density currents are fed by fine-grained particles and air that are expelled when coarser material sediments rapidly along the ray axis. Although we could not sample these fine-grained deposits, the videos record their formation. In natural volcanic explosions we expect that this process could result in lobate fines-rich deposits that thin away from a lobe's dispersal axis. They would be similar to lateral-blast deposits with fines-depleted basal layers and finer grained upper layers and evidence of traction carpet deposition. Additionally, isolated large clasts often travel at the tips of these jets, or on isolated paths beyond the distribution of the main body of the jet.

4.2 Ejection of shallow- versus deep-seated materials

Medial ejecta deposits were dominated by clasts from strata above the explosion sites (layers F, E, D, and aquarium gravel). Deposits from the initial blasts at Pads 1-3 were relatively enriched near the crater in material from layer D, which was progressively replaced by layer E material and aragonite with increasing distance. In other words, deep-seated materials were not ejected as far as shallow-seated materials. The medial ejecta componentry evolved with each subsequent blast. Clasts from deeper layers (but still above the explosion site) became enriched in the ejecta only after multiple blasts (Fig. 9). This is interpreted as due to progressive blast-driven mixing of materials within subcrater deposits, which form the overburden for subsequent explosions. While this is accompanied by a depletion of shallow clast types, collapse of the crater rim will return shallow and recently erupted material to the crater, where it might be re-ejected.

Proximal ejecta samples were collected from the crater wall, the high point of the crater rim, and the deposits just outside the crater rim. While there were limited samples of proximal ejecta (Pad 1, Pad 3 and Pad 5) the componentry show similarities to medial ejecta for these blasts. Some proximal samples included deeper materials (layer D, C, and B), but only one blast in these experiments ejected material excavated from the depth of the charge (Pad 1). This blast had a scaled depth that was approximately the optimal excavation value of ~0.004 m/J $^{1/3}$. While pads with multiple blasts excavated progressively deeper material, the ejecta containing material from the depth of charge placement was notably absent. This suggests that the ejection of deep lithics results from a complex explosive history with progressive upward mixing in the subsurface requiring later shallow blasts to enable eruption and deposition of the lithics outside the crater. Variable blast depth with time and subsequent mixing has been recently inferred from field data (Valentine 2012; LeFebvre et al., 2013), rather than progressive deepening of explosion sites (e.g., Lorenz, 1986).

4.3 Crater and Subcrater facies and geometry

Each blast produced either a broad crater, a retarc in a shallow depression, or a narrow steep-sided collapse pit. These record processes dominated by ejection of material from the explosion epicenter, by vertical lofting and fallback of material to the epicenter, or by *in situ* subsidence around the explosion site respectively. The surface structure, at most explosion epicenters, evolved in response to multiple explosions in the subsurface and collapses of the crater rim. Subcrater disruption profiles reveal areas of reduced compaction (i.e., deformation or damage) immediately beneath the crater and crater rim. The experiments produced disrupted areas that narrow with depth, and have relatively steep sides that extended below the depth of deepest charge placement for a given pad (similar to Ross et al., 2013). The average dips of the subcrater structures' walls, defined by the compaction profiles, ranged from 40 to 85 degrees. For single blasts, steeper structures resulted from deeper charges. When subsequent blasts produced wider craters the dips of the subcrater structure walls became progressively less steep. The depth of damage beneath the charge site increased with decreasing scaled depth. The diameter of the disruption area always exceeded the diameter of the crater as measured at the surface (Table 2), but typically corresponded with or was just outboard of evident deformation in the excavated subcrater deposits.

Two major facies were identified in the subcrater deposits: bedded subcrater facies, which, when present, occur immediately below the crater floor, and domainal subcrater facies beneath bedded subcrater deposits, if the latter were present. Bedded subcrater deposits were typically 3-10 cm thick and contained 0.5-3 cm-thick beds of homogeneously mixed aggregate and beds of unmixed material. The latter can be composed of material that originated just below the pad surface, or include material from as deep as 0.45 m below the original surface. These bedded deposits were thickest just beneath the crater bottoms and thinned toward the crater edges. The thickness of the bedded facies also varied circumferentially within the crater, corresponding to deposit rays observed at the surface. Bedded subcrater deposits were formed in

Pads 1-3, but they were best developed in Pad 3 where the scaled depth is greater than the optimal scaled depth (Fig. 6).

Domainal deposits formed the bulk of the subcrater structures, with domains including: (1) deformed subsurface material grading laterally into *in situ* pad layers, and (2) displaced subsurface material with steep to near-vertical boundaries. The margins of domainal subcrater deposits are distinguished by downward sagging of the pad layers. The gradational transition to undisturbed pad strata approximately paralleled the disruption profiles as measured by penetrometers. The central downward synformal sagging of the layers within the subcrater structures accompanied an increase in thickness of the layers at the centers of the structures, which commonly extended below the original pad layers into underlying aggregate (5-30 cm; see especially Pads 4, 5; Fig. 6). The structures resembled a series of stacked bowls with extreme over-thickening in the lowest units. The contacts between the deformed layers displayed irregular undulations a few centimeters apart, with amplitudes up to several centimeters (Fig. 6). Outside the central structures, tension cracks were locally present along the top of one unit, filled in with material from the overlying unit (3-5 cm deep; Ross et al. 2013). In some cases (Pad 1 and 3) the center of the structure contained concentric vertical domains that protruded upward from a deeper unit into shallower ones (see esp. Pad 3; Fig. 6).

Bedded subcrater deposits extended up to 20 cm below the pad surface, and lay immediately on top of a concentric domainal subcrater layer containing material from layers B, C, D and E (Fig. 7). No concentric upward-extending core was formed in the deep-blast experiment with co-located explosions (Pad 4). In the case of upward moving charges (Pad 5), however, detailed componentry data and field observations reveal incipient mixing of deep-seated material upward into subcrater deposits that are otherwise dominated by deformed shallow pad-layer material.

Deformation and mixing in the subsurface are related to upward and downward motion of materials relative to their original positions. Net upward motion was preserved in the vertically oriented, concentric, domainal deposits, similar to features recorded in diatreme structures under maar volcanoes (White 1991; Ross et al. 2013, LeFebvre et al. 2013). Upward migration of material is invoked as an important mixing process (White 1991), typically associated with debris jets (Ross and White 2006; Ross et al. 2008a, 2008 b; LeFebvre et al., 2013). Net downward motion was preserved in the synformal experimental structures, which were associated with the formation of subsidence pits, similar to those formed in contained nuclear explosion tests (Houser 1969). The steep dips of subcrater deposits implies that explosion-driven upward motion and syn-eruption subsidence are sufficient to form these dips and do not require post-eruption compaction to form (Geshi et al. 2011; Delpit et al. in review) although evidence for post-formational subsidence has been observed at some maar craters (e.g., Brand et al. 2009; Ross et al. 2011).

Upward movement in this system is driven by the disruption of the subsurface by rapid expansion of gas produced by the chemical explosive. This explosion-driven disruption affects material in all directions around the charge, including below the charge. The deposits produced by these experiments and by laboratory experiments (Ross et al. 2008a, 2008b) indicate that the displacement is dependent on scaled depth. It is only in shallow explosions that some material is displaced from the subsurface into the atmosphere and 'erupted.' Some of the erupted material may be deposited outside the crater, but much is deposited within the forming crater.

In the subsurface, the space produced by the gas expansion and by upward displacement of material is reoccupied by deposits once upward momentum of overlying material is expended. This reoccupation is accomplished through lateral and downward motion of layered pad material (inward slumping) and near-vertical deposition of material carried in an eruptive jet. After the deposition from the jet (fallback), additional displacement can occur in the form of subsidence of the material within and below the crater. Video recordings of the deep blasts show that there was a delay between depositional fallback of jet material and downward sagging of the surface, which occurred up to 2 seconds after deposition stopped (Pad 4 and 5). The formation of the subsidence pit without the production of ejecta represents an apparent decrease in volume of the pad surface, and in excavation the downward disruption of the pad layers appears to have an anomalous displacement of the mixed aggregate below the constructed layers. Compaction profiles indicate a decrease in the pad density, which should produce a volume increase (like a retarc), so these conditions require deformation of the surrounding pad that was not directly detected by excavation. The potential for explosions to increase the density of material outside the immediate subcrater structure was revealed by the upward migrating compaction profiles in Pad 5. Changes in the thickness of aggregate layers near the base and lateral margins of the subcrater structure are likely important to this change in compaction of the subsurface. These variations likely are controlled by material properties including sorting and (though not tested here) saturation. The displacement of the mixed gravel and the dynamic nature of the disrupted pad density indicate the complexity of the subcrater structure as a product of multiple explosions and will be considered in future experiments.

The experiments indicate that bedded subcrater deposits only form when there is lofting of material above the pad surfaces; the thickness of bedded deposits increased with repeated blasts and involved recycling of previous fallback material. Significant recycling accompanies the formation of primary bedded subcrater deposits in natural maar-diatremes (Houghton and Smith 1993; Lefebvre et al., 2013). In these experiments componentry analyses indicate that bedded subcrater deposits experienced greater mixing than deeper deposits. This may be influenced by the small number of blasts used in these experiments. However, and in contrast to the ejecta (extracrater) deposits, the bedded subcrater deposits from multiple explosions do include clasts from the depth of explosion. Similar, but less well-developed bedded subcrater deposits were produced in previous experiments, where only two, thick (30 cm) layers were present in the pads (Ross et al. 2013). The development of recognizable stratification in the sub-crater deposits is probably dependent on the range of clast types, number of pad layers, and clast sizes in the pad strata, as reflected by the differences between these two experimental sets.

5.0 Application to maar-diatremes

The effect of increasing scaled depth on the transition from crater to retarc to subsidence pit has been well documented for underground nuclear weapons tests (Benning and Kurtz 1967; Houser 1969; Gould et al. 1981), and were replicated the these experiments. Nuclear tests involved energies six to nine orders of magnitude larger than our experimental blasts, overlapping and exceeding the range of energies of realistic volcanic explosions at natural maars (Self et al. 1980; Taddeucci et al. 2010; Valentine et al. 2011; Valentine and White 2012). An additional potential scaling issue is the ‘detonation’ wave speeds of volcanic explosions. Phreatomagmatic (molten fuel-coolant interaction) explosions have been studied experimentally (Büttner and Zimanowski, 1998) with wave speeds that are slower than those of chemical explosives used in our experiments. Nuclear tests have very different detonation speeds from those of our chemical explosions but the general phenomena are the same. This similarity indicates that different detonation speeds do not strongly influence crater and ejecta phenomena, consistent with Goto et al. (2001). The consistency between features of our experiments and those of nuclear tests with similar scaled depths (see Houser 1969) lends further credence to the arguments of Ross et al (2013) that our experiments are well scaled for the reproduction of key volcanic explosion phenomena.

Ejecta produced by shallow blast experiments are dominated by material from near-surface pad layers similar to observations of maar-diatreme volcanoes (Ross et al. 2011; Valentine 2012; Lefebvre et al. 2013). Deeper-seated material, when present, was deposited near the crater, with progressively shallower material increasing in abundance with distance from the crater (cf. Lee and Mazzola 1989; Table 3). Materials from greater depths can be included in more distal deposits after repeated blasts in the same crater have mixed subcrater deposits and are ejected by later shallow explosions (Fig. 9). This mixing by repeated blasts in natural maars would produce both a lateral and vertical trend deposit composition, in which materials from deeper stratigraphic units are deposited close to the vent early in the eruption, but may be found in more distal parts of later deposits. Inverse vertical lithic-fragment stratigraphy has been observed in tephra rings of historical and eroded maar volcanoes (Kienle et al. 1980; Self et al. 1980; White 1991). Proximal deposits can be lost as a maar crater grows, so that portions of this pattern are missing from the geologic record, because of syn- and post-eruptive collapse of the crater rim. Furthermore, as a crater develops it acts to focus eruptive jets vertically, so that most of their material falls back into the crater. This promotes mixing of materials in the shallow part of a diatreme but reduces the chance of those materials ending up in tephra ring deposits.

Because only shallow blasts successfully eject material from the crater, ejecta componentry reflects a combination of clast recycling and subsurface mixing from repeated explosions at various depths. A common assumption is that lithics in tephra ring deposits around maars record explosions at the lithics' depth of origin (e.g., Sheridan and Wohletz 1983; Lorenz 1986; Mattson et al. 2005; Carrasco-Núñez et al. 2007; Sottili et al. 2009, 2012; Jordan et al. 2013; van Otterloo et al. 2013). Only one of the experimental blasts (Pad 1), which was at the optimal depth of burial for crater excavation and had a flat undisrupted pad surface, ejected material from the charge depth. While it is true that the presence of a deep-seated lithic can imply that there was an explosion at its source depth, it is unlikely that the same explosion ejected the lithic fragment from the crater. Instead, we infer that such lithics are gradually driven upward in the diatreme, in stages, by the phenomenon of debris jetting (Ross and White 2006; Ross et al. 2008a, 2008b), until a shallow explosion ejects it. This inference is supported both by these experiments and by recent studies of maars and diatremes where there are good constraints on lithic source depths (Valentine 2012; Lefebvre et al 2013). An important implication of these results is that the appearance of progressively deeper-seated lithics high in the stratigraphy of a tephra ring does not record deepening of phreatomagmatic explosion sites due to drawdown of the water table (Lorenz 1986). Rather, the late eruption of more deeply sourced lithics is related to the time and number of repeated explosions of varying energies and depths needed to drive the lithic into the upper part of the diatreme with later shallow blasts to eject the lithics out of the crater (Valentine and White 2012). Further examples of this process of driving lithics upward is supported by the observation of maars in the Colli Albani Volcanic District (Central Italy), where a higher degree of rounding and fragmentation experienced by deeper-derived lithics in comparison to shallower-derived ones reflects a longer period of intra-conduit mixing and milling before ejection (Sottili et al. 2009), and in phreatomagmatic deposits at Easy Chair volcano in Nevada (USA; Valentine and Cortés, 2013). Similarly, the absence of deep-seated lithics in a tephra ring does not imply a lack of deep explosions, just that debris from those deep explosions was not sufficiently driven upward before the eruptive episode ended nor successfully ejected from the crater by later shallow blasts. Ejecta beds (or bed sets) only record shallow scaled depth explosions in tephra ring deposits and can be used to estimate minimum numbers of explosions. Crustal lithics may be used to constrain only minimum depths of explosive activity within the growing system over its growth history, and not at a specific time.

Our experiments reveal a diversity of jet shapes and resulting ejecta deposits, which are influenced by the position of the explosion and the pad compaction and overlying topography (flat, crater, or retarc; Figure 12). Natural systems also reveals a diversity of tephra ring deposits around maar-diatremes: (1) coarse-grained (tuff breccia to lapilli tuff), poorly-sorted massive deposits that may be related to direct and rapid sedimentation from an eruptive jet; (2) finer-grained (lapilli tuff to tuff), moderately-sorted, bedded and cross bedded deposits from dilute pyroclastic density currents; (3) distal ballistics and fine ash fall (Fisher and Waters 1970; Waters and Fisher 1971; Crowe and Fisher 1973; Schmincke et al. 1973; Self et al. 1980; Sohn and Chough 1989; Chough and Sohn 1990; Valentine 2012; Jordan et al. 2013; van Otterloo et al. 2013). Differences between these deposits have previously been interpreted in terms of distance from the blast source and/or as the result of different explosion mechanisms (e.g., phreato-Vulcanian, Ukinrekian; van Oterloo et al., 2013), but experiments reveal that this diversity could also be related to scaled depth of explosions, the nature of the existing crater (if present), and the heterogeneous nature of the eruptive jets. For example, the presence of a poorly sorted, and massive lapilli tuff or tuff breccia in a tephra ring sequence (e.g., Valentine and

Cortés, 2013) may be related not to a fundamentally different type of explosion, but to a very shallow scaled depth and/or absence of a deep crater (Figure 12a), or by jets that are directed laterally by the presence of a retarc (Figure 12b). Finer-grained dune-bedded tephra ring deposits may be caused by a vertically focused eruptive jet, because of large scaled depth or confinement by a crater, where most of the mixture collapses back onto the explosion epicenter but a cloud of fines and gas (air) is expelled from the collapsing mixture to feed a dilute density current (e.g., P3B3 and P5B2 blasts and Valentine et al., 2012; Figure 12c). We infer that collapsing, high-particle-concentration fingers might produce deposits similar to those from lateral blast deposits (Belousov et al., 2007) but more localized and not related to a lateral blast *sensu stricto* (Figure 12d).

In addition to craters and ejecta, the blasts successfully produced complex subsurface mixing driven by both subsidence (Hearn 1968) and explosion-driven upward mixing (debris jets; Ross et al. 2006, 2008; Valentine 2012). The deposits formed by the explosion-driven mixing were dependent on the scaled depth, with shallow blasts producing bedded subcrater deposits, and deep blasts contributing to the formation of domainal subcrater deposits. Bedded, primary subcrater deposits like those here (Pad 1-3) are known from exhumed maar-diatreme structures like Missouri River Breaks, Montana and Suona Crater, Miyakejima (Geshi et al. 2011; White and Ross 2011; Delpit et al. in review) as well as kimberlite pipes such as Mwadui kimberlite (Stiefenhofer and Farrow 2004). In our experimental structures the best-developed vertical domains in the domainal subcrater deposits were produced by fairly shallow blasts near or just below the optimal scaled depth (Pad 1-3), whereas deeper blasts (Pads 4-5) initiated subsurface mixing from multiple blasts below the optimal depths of burial.

The Suoana maar-diatreme is revealed in natural cross-section in the caldera wall of Miyakejima volcano (Geshi et al. 2011) and provides an excellent comparison with our experimental ‘maar-diatremes’ (Fig 13). Both structures have bedded proximal deposits, bedded subcrater deposits, and domainal subcrater deposits. Suoana Crater has four proximal tephra layers, which suggest that a minimum of four shallow explosions formed the maar-diatreme, potentially similar to the three blasts of the Pad 3 experiment. The boundaries of the subcrater 'diatreme structures' both here and for Suona (Fig. 13) have subsidence along the margin of the structure. Although Suona displays well-developed fractures, the relative size, deposit types, and internal structures are highly similar.

6.0 Conclusions

The experiments presented here were analogs for subsurface volcanic explosions with different strengths and positions that produce both subsurface and surface deposits. Appropriate scaling with natural volcanic explosions is indicated by successful reproduction of structures and landforms similar to those of maar-diatreme volcanoes (White and Ross 2011). Jet heights and shapes, and resulting deposition of ejecta, were determined primarily by scaled depth and the condition of the pad (compacted with no topography or disrupted with a crater or retarc) above the explosion. Large scaled depths and the presence of a crater both act to vertically focus eruptive jets and promote collapse back onto the explosion epicenters. Component analyses show that ejecta deposits are dominated by materials that originated above (rarely at) the explosion site, and that shallower-seated materials are deposited farther from the craters than are deep-seated materials. Extracrater deposits are only produced by shallow blasts that eject material from the near surface that may include crustal lithics that have been moved upward through subsurface mixing by previous deeper explosions. Subcrater deposits comprise bedded upper parts and domainal lower parts, both of which record mixing of materials from various depths (mainly above explosion sites). The presence or absence of deep-seated material in ejecta is not directly related to the depth of a given explosion and those lithics present represent only a minimum fragmentation/explosion depth. Ejection and deposition processes observed in the experimental blasts indicate the potential for a range of different tephra ring deposition processes (fall and flow) simply due to differences in scaled depths of explosions and the pre-explosion topography.

The experiments reported here and in Valentine et al. (2012), Taddeucci et al. (2013), and Ross et al. (2013), represent a simplified scenario with vertically aligned explosion locations. Many natural maars show evidence of horizontally migrating or/and multiple coalescing vents laterally (e.g. Ort and Carrasco-Núñez 2009; Jordan et al. 2013; Nemeth et al. 2012; Son et al. 2012; van Otterloo et a. 2013), which will be the topic of further experimentation. Experiments to date reveal important trends in the effects of subsurface explosions, where the most significant hazards show a trend of ‘peak’ behavior with optimal scaled depth: ejecta distance, duration of jet (deposition time), and crater size. Such integrated experimental deposits are necessary to improve our models of natural phenomena.

7.0 Acknowledgments

These experiments were funded primarily by the University at Buffalo through the UB Center for Geohazards Studies, with additional contributions from team member sponsors (including NSERC: Discovery grant to P.-S.R), and were conducted at the Geohazards Field Station. M. Manoranjan, B. Zimanowski, A. Schmid, D. Gaudin, D. Bowman, K. Keehoon, U. Kueppers, and G. Lube are thanked for their participation in this project. We also thank the following for their key assistance in preparing for and executing the experiments: D. Goralski, J.L. Ball, K. Bennet, D. Doronzo A.G. Harp, C.G. Hughes, P. Johnson, S. Pansino, D. Ruth, D. Schonwalder, M. Sweeney, and P. Moretti. The manuscript was improved through helpful reviews by B. Brand and Y.K. Sohn.

7.0 References

Belousov, A. (2006), Distribution and eruptive mechansim of maars in the Kamchatka Peninsula, *Doklady Earth Sciences*, *406*, 24-27.doi:10.1134/S1028334X06010077.

Bening, R. G., and M. K. Kurtz (1967), The formation of a crater as observed in a series of laboratory- scale cratering experiements*Rep.*, p. 63 pp, U.S. Army Engineer Nuclear Cratering Group, Livermore CA.

Brand, B. D., and A. B. Clarke (2009), The architecture, eruptive history, and evolution of the Table Rock Complex, Oregon: From a Surtseyan to an energetic maar eruption, *Journal of Volcanology and Geothermal Research*, *180*, 203-224. doi: 10.1016/j.jvolgeores.2008.10.011.

Brand, B.; Clarke, A.; Semken, S. (2009), Eruptive conditions and depositional processes of Narbona Pass Maar volcano, Navajo volcanic field, Navajo Nation, New Mexico (USA), *Bulletin of Volcanology*, 71, 49-77. DOI: 10.1007.s00445-008-0209-y.

Büchel, G., and V. Lorenz (1993), Syn- and post-eruptive mechansim of the Alaskan Ukinrek Maars in 1977, *Lecture Notes in Earth Sciences*, *49*, 15-60.

Büttner, R., and B. Zimanowski (1998), Physics of thermohydraulic explosions, *Physical Review 57*, 5726-5730.

Carrasco-Núñez, G., M. H. Ort, and C. Romero (2007), Evolution and hydrological conditions of a maar volcano (Atexcac crater, Eastern Mexico), *Journal of Volcanology and Geothermal Research*, *159*, 179-197. doi: 10.1016/j.jvolgeores.2006.07.001.

Chough, S. K., and Y. K. Sohn (1990), Depositinal mechanics and sequences of base surges, Songaksan tuff ring, Cheju Island, Korea, *Sedimentology*, *37*, 1115-1135.

Delpit, S., P.-S. Ross, and B. C. Hearn (in review), Deep bedded ultramafic diatremes in Missouri River Breaks volcanic field, Montana, USA: more than 1 km of syn-eruptive subsidence, *Bulletin of Volcanology*.

Fisher, R. V., and A. C. Waters (1970), Base surge bed forms in maar volcanoes, *American Journal of Science*, *268*, 157-180.

Geshi, N., K. Németh, and T. Oikawa (2011), Growth of phreatomagmatic explosion craters: A model inferred from Suoana crater in Miyakejima Volcano, Japan, *Journal of Volcanology and Geothermal Research*, *201*, 30-38. doi: 10.1016/j.jvolgeores.2010.11.012.

Goto, A., and H. Taniguchi (2001), Effects of explosion energy and depth to the formation of blast wave and crater: Field explosion experiment for the understanding of volcanic explosion, *Geophysical Research Letters*, *28*, 4287-4290.

Gould, K., and K. Tempo (1981), High-explosive Field Tests: Explosion phenomena and environmental impacts*Rep.*, Defense nuclear agency Santa Barbara, California.

Hearn, C. B. (1968), Diamteres with Kimberlitic affinities in North-Central Montana *Science*, *159*(3815), 622-625.

Houghton, B. F., and R. T. Smith (1993), Recycling of magmatic clasts during explosive eruptions: estimating the true juvenile content of phreatomagmatic volcanic deposits, *Bulletin of Volcanology*, *55*, 414-420.

Houser, F. N. (1969), Subsidence related to underground nuclear explosions, Nevada Test Site, *Bulletin of the Seismological Society of America*, *59*(6), 2231-2251.

Jordan, S. C., R. A. F. Cas, and P. C. Hayman (2013), The origin of a large (>3 km) maar volcano by coalescence of multiple shallow craters: Lake Purrumbete maar, southeastern Australia *Journal of Volcanology and Geothermal Research*, *254*, 5-22. doi: 10.1016/j.jvolgeores.2010.11.012.

Kienle, J., P. R. Kyle, S. Self, R. J. Motyka, and V. Lorenz (1980), Ukinrek Maars, Alaska, I. April 1977 eruption sequence, petrology and tectonic setting, *Journal of Volcanology and Geothermal Research*, *7*, 11-37.

Kwon, C. W., and Y. K. Sohn (2008), Tephra-filled volcaniclastic neck (diatreme) of a mafic tuff ring at Maegok, Miocene Eoil Basin, SE Korea, *Geosciences Journal*, *12*(4), 1-13. doi: 10.1007/s12303-008-0032-7.

Lee, C. K. B., and T. A. Mazzola (1989), Ejecta scaling laws for craters in dry alluvial sites, *Journal of Geophysical Research*, *94*, 17595-17605.

Lefebvre, N. S., J. D. L. White, and B. A. Kjarsgaard (2013), Unbedded diatreme deposits reveal maar-diatreme forming eruptive processes: Standing Rocks West, Hopi Buttes, Navajo Nation, USA, *Bulletin of Volcanology*, *75*, 739. doi: 10.1007/s00445-013-0739-9.

Lorenz, V. (1986), On the growth of maars and diatremes and its relevance to the formation of tuff rings, *Bulletin of Volcanology 48*, 265-274.

Lorenz, V., and S. Kurszlaukis (2007), Root zone processes in the phreatomagmatic pipe emplacement model and consequences for the evolution of maar-diatreme volcanoes, *Journal of Volcanology and Geothermal Research*, *159*, 4-32. doi: 10.1016/j.jvolgeores.2006.06.019.

Lutz, H., V. Lorenz, T. Engel, F. Häfner, and J. Haneke (2013), Paleogene phreatomagmatic volcanism on the western main fault of the northern Upper Rhine Graben (Kisselwörth diatreme and Nierstein-Astheim Volcanic System, Germany), *Bulletin of Volcanology*, *75*, 741-755. doi: 10.1007/s00445-013-0741-2.

Melosh, H. J. (1989), *Impact Cratering. A Geologic Process*, Clarendon Press. , Oxford.

Ohba, T., H. Taniguchi, H. Oshima, M. Yoshida, and A. Goto (2002), Effect of explosion energy and depth on the nature of explosion cloud. A field experiemental study *Journal of Volcanology and Geothermal Research*, *115*, 33-42.

Ort, M. H., and G. Carrasco-Núñez (2009), Lateral vent migration during phreatomagmatic and magmatic eruptions at Tecuitlapa Maar, east-central Mexico, *Journal of Volcanology and Geothermal Research*, *181*, 67-77. doi: 10.1016/j.jvolgeores.2009.01.003.

Ross, P. S., and J. D. L. White (2006), Debris jets in continental phreatomagmatic volcanoes: A field study of their subterranean deposits in the Coombs Hills vent complex, Antarctica *Journal of Volcanology and Geothermal Research*, *149*, 62-84. doi: 10.1016/j.jvolgeores.2005.06.007.

Ross, P. S., J. D. L. White, B. Zimanowski, and R. Büttner (2008)a, Multiphase flow above explosion sites in debris-filled volcanic vents: Insights from analogue experiments, *Journal of Volcanology and Geothermal Research*, *178*, 104-112. doi: 10.1016/j.jvolgeores.2008.01.013.

Ross, P.-S., J. D. L. White, B. Zimanowski, and R. Büttner (2008)b, Rapid injection of particles and gas into non-fluidized granular material, and some volcanological implications *Bulletin of Volcanology*, *70*, 1151-1168. doi: 10.1007/s00445-008-0230-1.

Ross, P.-S., S. Delpit, M. J. Haller, K. Németh, and H. Corbella (2011), Influence of the substrate on maar-diatreme volcanoes- An example of a mixed setting from the Pali Aike volcanic field, Argentina, *Journal of Volcanology and Geothermal Research*, *201*, 253-271. doi: 10.1016/j.jvolgeores.2010.07.018.

Ross, P.-S., J. D. L. White, G. A. Valentine, J. Taddeucci, I. Sonder, and R. Andrews (2013), Experimental birth of a maar-diatreme volcano, *Journal of Volcanology and Geothermal Research*, *260*, 1-12. doi: 10.1016/j.jvolgeores.2013.05.005.

Schmincke, H.-U., R. V. Fisher, and A. C. Waters (1973), Antidune and chute and pool structures in the base surge deposits of the Laacher See area, Germany, *Sedimentology*, *20*, 553-574.

Self, S., J. Kienle, and J.-P. Huot (1980), Ukinrek Maars, Alaska, II. Deposits and formations of the 1977 craters, *Journal of Volcanology and Geothermal Research*, *7*, 39-65.

Sohn, Y. K., and S. K. Chough (1989), Depositional processes of the Suwolbon tuff ring, Cheju Island (Korea), *Sedimentology*, *36*, 837-856.

Son, M., J. S. Kim, S. Jung, J. S. Ki, M.-C. Kim, and Y. K. Sohn (2012), Tectonically controlled vent migration during maar-diatreme formation: An example from a Miocene half-graben basin in SE Korea, *Journal of Volcanology and Geothermal Research*, *223-224*, 29-46. doi: 10.1016/j.jvolgeores.2012.02.002.

Sottili, G., J. Taddeucci, D. M. Palladino, M. Gaeta, P. Scarlato, and G. Ventura (2009), Sub-surface dynamics and eruptive styles of maars in the Colli Albani Volcanic District, Central Italy, *Journal of Volcanology and Geothermal Research*, *180*, 189-202. doi: 10.1016/j.jvolgeores.2008.07.022.

Sottili, G., D. M. Palladino, M. Gaeta, and M. Masotta (2012), Origins and energetics of maar volcanoes: examples from the ultrapotassic Sabatini Volcanic District (Roman Province, Central Italy), *Bulletin of Volcanology*, *74*, 163-186. doi: 10.1007/s00445-011-0506-8.

Stiefenhofer, J., and D. J. Farrow (2004), Geology of the Mwadui kimberlite, Shinyanga district, Tanzania *Lithos*, *76*, 139-160. doi: 10.1016/j.lithos.2004.04.017.

Taddeucci, J., G. A. Valentine, I. Sonder, J. D. L. White, P.-S. Ross, and P. Scarlato (2013), The effect of pre-existing crater on the initial development of explosive volcanic eruptions: An experimental investigation, *Geophysical Research Letters*, *40*, 507-510. doi:10.1002/grl.50176.

Valentine, G. A. (2012), Shallow plumbing systems for small-volume basaltic volcanoes, 2: Evidence from crustal xenoliths at scoria cones and maars, *Journal of Volcanology and Geothermal Research*, *223-224*, 47-63. Corrigendum *239-240*, 111-114. doi: 10.1016/j.jvolgeores.2012.01.012.

Valentine, G.A., and J.A. Cortés (2013) Time and space variations in magmatic and phreatomagmatic eruptive processes at Easy Chair (Lunar Crater Volcanic Field, Nevada, USA), *Bulletin of Volcanology, 75*, 752. doi: 10.1007/s00445-013-0752-z.

Valentine, G. A., and J. D. L. White (2012), Revised conceptual model for maar-diatremes: Subsurface processes, energetics, and eruptive products, *Geology*, *40*(12), 1111-1114. doi: 10.1130/G33411.1.

Valentine, G.A., Shufelt, N.L., and A.R.L. Hintz (2011) Models of maar volcanoes, Lunar Crater (Nevada, USA), *Bulletin of Volcanology, 73,* 753-765. doi: 10.1007/s00445-011-0451-6.

Valentine, G. A., J. D. L. White, P.-S. Ross, J. Amin, J. Taddeucci, I. Sonder, and P. J. Johnson (2012), Experimental craters formed by single and multiple buried explosions and implications for volcanic craters with emphasis on maars, *Geophysical Research Letters*, *39*, L20301. doi:10.1029/2012GL053716.

Waters, A. C., and R. V. Fisher (1971), Base surges and their deposits: Capelinhos and Taal Volcanoes, *Journal of Geophysical Research*, *76*(23), 5596-5614.

White, J. D. L. (1991), Maar-diatreme phreatomagmatism at Hopi Buttes, Navajo Nation (Arizona), USA, *Bulletin of Volcanology*, *53*, 239-258.

White, J. D. L., and P. S. Ross (2011), Maar-diatreme volcanoes: A review, *Journal of Volcanology and Geothermal Research*, *201*, 1-29. doi:10.1016/j.jvolgeores.2011.01.010.

Table 1: Summary of results about crater morphology, jet shape and duration.

Pad	Charge number	Charge size (kg)	Scaled depth [a] m/$J^{1/3}$	Depth of charge relative to pad (m)	Crater diameter (average) d (m)	Crater depth (max) h (m)[b]	Height of retarc above pad (max) (m)	h/d	Rim height above pad (average) (m)	Jet shape Wt/Wb[c]	Max jet height (m)	Deposition duration (s)	Greatest distance of ejecta [d]
1	1	0.45	3.8 x10^{-3}	0.5	1.70	0.37	-	0.21	0.06	2.12	14.1	3.0	17
2	1	0.3	4.4 x10^{-3}	0.5	1.53	0.30	-	0.20	0.03	1.47	8.3	2.75	15
	2	0.3	2.0 x10^{-3}	0.5	1.91	0.54	-	0.28	0.09	1.78	8.4	1.93	19
3	1	0.15	5.5 x10^{-3}	0.5	1.80	0.06	0.27	0.03	0.03	0.77	1.7	1.29	2
	2	0.15	5.5 x10^{-3}	0.47	1.37	0.31	-	0.23	0.08	1.37	1.1	0.48	4
	3	0.15	5.5 x10^{-3}	0.74	1.60	0.26	-	0.16	0.08	0.96	3.0	1.96	4
4	1	0.15	1.1 x10^{-2}	1	0.45	0.10[e]	-	0.21	0.02	0.29	0.3	0.24	-
	2	0.15	9.8 x10^{-3}	1	0.80	0.12[e]	-	0.15	0.01	0.30	0.3	0.22	-
	3	0.15	9.8 x10^{-3}	1	0.89	0.17[e]	-	0.19	0.03	0.51	0.3	0.16	-
5	1	0.15	1.1 x10^{-2}	1	0.58	0.09[e]	-	0.16	0.01	0.20	0.3	0.21	-
	2	0.15	7.9 x10^{-3}	0.8	1.08	0.05[e]	0.8	0.04	0.02	0.15	0.7	0.55	-
	3	0.15	6.3 x10^{-3}	0.5	1.32	0.37	-	0.28	0.04	1.40	1.9	1.15	3

a= scaled depth is the physical depth of burial divided by the cube root of the energy

b = crater depth from the raised rim
c = Wt/Wb is the ratio of the width of the top of the jet over the width of the base of the jet
d = expressed as multiples of crater radius
e = subsidence pit

Table 2: Measurements pertaining to the subcrater structures.

	Deepest charge (m)	Crater depth (m)[a]	Depth of disruption (m)	Depth of disruption below charge (m)	Diameter of subcrater structure (m)[b]	Ws-Wc/ Wc[c]	Slope angle of subcrater structure
P1B1	0.5	0.31	0.81	0.31	2.00	0.22	68
P2B2	0.5	0.45	0.84	0.34	2.05	0.07	51
P3B3	0.75	0.18	1	0.27	2.00	0.29	39
P4B1	1.0	0.08	1.16	0.16	0.90	1.14	72
P4B2	1.0	0.08	0.98	-0.02[d]	1.60	1.00	63
P4B3	1.0	0.14	1.21	0.21	1.25	0.42	51
P5B1	1.0	0.12	1.28	0.28	0.8	1.0	85
P5B2	0.8	-0.01	1.2	0.4	1.5	0.46	55
P5B3	0.5	0.32	0.88	0.38	1.7	0.31	50

a = a negative value indicates a mound

b= measured along the greatest width of the penetration profile

c = Ws-Wc/Wc is a ratio reflecting the excess of the subcrater structure relative to the crater diameter.

d= an anomalous value for this penetrometer run may have resulted from the penetrometer striking a stone.

Table 3: Deposit types compared to natural examples

Deposit type	Comparison	Location	Reference	Comments
Distal ejecta and medial	Ejecta blankets composed of ash fall, density current deposits and isolate blocks and bombs.	Albano Maar; Rotomahana; Ukinrek; Mt. Gambier; Teshim Maar (Hopi Buttes, USA); Military blast testing	Giaccio et al. 2007; Lee and Mazzola, 1989; Gould 1981; Benning and Kurtz 1967; Büchel and Lorenz 1993; van Otterloo et al. 2013	Material that is deposited beyond the scope of the collapsing crater and dominated by shallow dips.
Proximal ejecta	Tephra ring	Yangpori (S.Korea); Albano Maar, Fekete-hegy (Hungary); Lunar Crater (USA)	Auer, et al. 2007; White 1991; Lefebvre et al. 2013; Giaccio et al. 2007; Sohn and Chough, 1989; Chough and Sohn, 1990; Valentine et al. 2011	Subject to collapse during crater growth, likely poor preservation of initial deposits.
Bedded subcrater deposits	Bedded diatreme, upper diatreme	Missouri River Breaks (Montana)	Hearn 1968; White and Ross 2011; Delpit et al. in review; Son et al. 2012	Not always present.
Domain-dominated subcrater deposits	Un-bedded diatreme, Lower diatreme	Hopi Buttes; Suoana Crater	Kwon and Sohn 2008; Lefebvre et al. 2012; Lefebvre et al. 2013; White 1991; White and Ross 2011; Ross et al. 2013; Geshi et al. 2011	Product of both subsidence and explosion-driven upward motion.

* Collapse pits are not preserved at Maar volcanoes, but the occurrence of these pits in the experiments represents the subsidence that plays a key role in maar and diatreme development.

FIGURE CAPTIONS

Figure 1: Schematic of pad set up including sampling bins. Experimental pad set up A) map view, showing sample boxes, pad spacing and camera positions. B) Cross-section of pits containing experimental pads to show pre-blast stratigraphy. Pads 1-3 used layers B-F and Pads 4-5 used A-F. Aquarium gravel was used to fill the charge hole after the charge was placed. Previous experiments (Valentine et al. 2012; Ross et al. 2013; Taddeucci et al. 2013) had a broad mounded pad surface.

Figure 2: Image captures of the peak jet shape from high definition video of blasts from Pad 1 and Pad 2. For each blast jet shape, resulting crater, and probe profiles are included. The dimensions of the jet width of top/width of bottom (Wt/Wb) are listed on the upper right hand corner. Charge location is located on the probe profiles. Schematic of a generalized plume with the parameters used to define the jets (Wt/Wb and height) is included.

Figure 3: Post-blast pad surfaces for each blast, as indicated by Pad and Blast number. Black marks on vertical scales are 10 cm and black scales on the wall in the background are 1 m in length.

Figure 4: Mass per unit area for experimental pads. A) Comparison of ejecta from Pads 1-3 highlighting the change resulting from subsequent blasts. P2B2 interacted with a crater, P3B2 interacted with a retarc. The videos revealed that due to billowing of the sample bags for P1B1 some volume of ballistic samples were not collected in the first sample bins for P1B1. This means that mass values for these first bin is considered a minimum value. B) Pads 1-3 overlapping with a logarithmic scale to highlight the increased variation that occurs in the distal eject noted with dashed line (<0.1 kg/m2). C) Comparison of initial blasts through undisturbed pads from 2013 to 2012 (Valentine et al. 2012).

Figure 5: Concentration (mass per unit area) of medial and distal ejecta for Pads 1 and 2. Componentry at several positions from the blast center are presented in histograms of weight percent concentration. Stratigraphic layers are B-F in order from bottom to top, and aquarium gravel was used to fill the charge hole.

Figure 6 Excavation cross-sections of blast sites for all pads. Colors represent different components that are consistent throughout the figures. Sample locations and blast positions are noted along with final penetrometer profiles. Detailed images and schematics are provided for proximal ejecta, bedded subcrater deposits and a map view of domainal subcrater deposits are included. Fine detail of surface morphology was not preserved between the formation of the craters and excavation due to protective tarps and precipitation.

Fig. 7: Simple map showing the spatial distribution of materials in subcrater deposits as they would be exposed with the removal of subcrater deposits and ejecta. This highlights the concentric nature of the deformation and dominance of shallow units in these structures.

Figure 8: Image captures from high definition video of Pads 3-5. For each blast jet shape, resulting crater, and probe profiles are included. The dimensions of the jet width of top/width of bottom (Wt/Wb) are listed on the upper right hand corner. Charge location is located on the probe profiles. Scales have 10 cm vertical increments. The legend is found on Figure 2.

Figure 9 Componentry of medial ejecta from Pad 2 and Pad 3 reflecting the evolution of the ejecta with each subsequent blast.

Figure 10 Jet properties compared with scaled depth A) jet height, B) duration of deposition and C) distance of distal and medial ejecta. Distal ejecta distribution and duration of deposition both peak at the optimal scaled depth (highlighted by the black line). The distance of distal ejecta collection, however, continues to increase with decreasing scaled depth (highlighted by the black line). The shaded area represents the scaled depth range for optimal crater excavation. C) Includes data from previous studies (Valentine et al 2012 and unpublished data), and data from Bening and Kurtz 1967 single blast cratering experiment are included for comparison.

Figure 11 Relationship between jet shape (width of top of jet over the width of the base) and distance of deposition. While there is some scatter, the wider the jet, the greater the distribution of ejecta. Jets with a Wt/Wb < 0.5 produce no ejecta.

Figure 12 Cartoon schematics of ejection (left) and deposition (right) processes observed in the experiments. Black objects represent relatively coarse clasts. Gray shades represent mixtures of particles and gas, with darker shades representing concentrated and relatively poorly sorted mixtures, and light shades representing dilute and fine-grained mixtures. Arrows represent direction of motion during ejection and deposition. (a) Optimal to shallow scaled depth with flat pre-blast topography. (b) Blast beneath a retarc (mound) with ejecta directed laterally around the topographic high. (c) Blast with depth greater than optimal scaled depth and/or beneath a pre-existing crater. (d) Detailed side and top views of depositional phase of a clast-rich finger from an erupted jet.

Figure 13: Comparison of a natural example of a small maar-diatreme in cross-section from Miyakejima Japan (image courtesy of Nobuo Geshi) with Pad 3 from these experiments. The schematic shows (not to scale) the similar and dissimilar features of the two sections. Detailed descriptions of the Suoana Crater, Miyakejima are available in Geshi et al. 2011. The host rock of Suona crater is alternating pyroclastic deposits and lesser lava.

Supplementary Material:

Supplementary table 1: Grain size data for aggregates used in the experiments.

Layer	Mean (mm)	Mode (mm)	Sorting		Maximum grain size (mm)	Skewness		Bulk Density g/cm^3	Material type
E	1.03	2.8	1.5	poor	4	-0.4	fine skewed	1.3	Crushed limestone
D	11.03	22.6	1.3	moderate	16	-0.6	fine skewed	1.5	Recycled asphalt
C	0.76	0.4	1.4	moderate	4	0.2	coarse skewed	1.6	Concrete sand
B	4.59	5.7	0.6	mod well	16	-0.5	fine skewed	1.4	Limestone pea gravel
A	6.20	5.7	1.2	moderate	8	-0.6	fine skewed	1.4	Red landscaping gravel
AqG	9.11	8.0	0.6	mod well	8	-0.4	fine skewed	1.4	Aquarium gravel

Video 1:

High definition video of Pad 1 Blast 1 where a 0.45 charge was detonated at a depth of 0.5 cm (optimal scaled depth) in an undisturbed pad with no topography. Black and white scale bars have increments of 10 cm and horizontal black lines on the concrete wall are 1 m long.

Video 2:

High definition video of Pad 2 Blast 2 where the charge was detonated beneath an existing crater in a disrupted pad (0.3 kg charge at 26 cm below the crater bottom, low scaled depth). Black and white scale bars have increments of 10 cm and horizontal black lines on the concrete wall are 1 m long.

Video 3:

High speed video (300 frames per second) of Pad 3 Blast 2 where the charge was detonated beneath a retarc (mound) that was produced by a previous blast (0.15 kg charge at 50 cm below the top of the retarc). Black and white scale bars have increments of 10 cm and horizontal black lines on the concrete wall are 1 m long.

Video 4:

High speed video (300 frames per second) of Pad 4 Blast 1 where the charge was detonated in an undisturbed pad with no topography, well below the optimal scaled depth (0.15 kg charge at 1 m). Black and white scale bars have increments of 10 cm and horizontal black lines on the concrete wall are 1 m long.

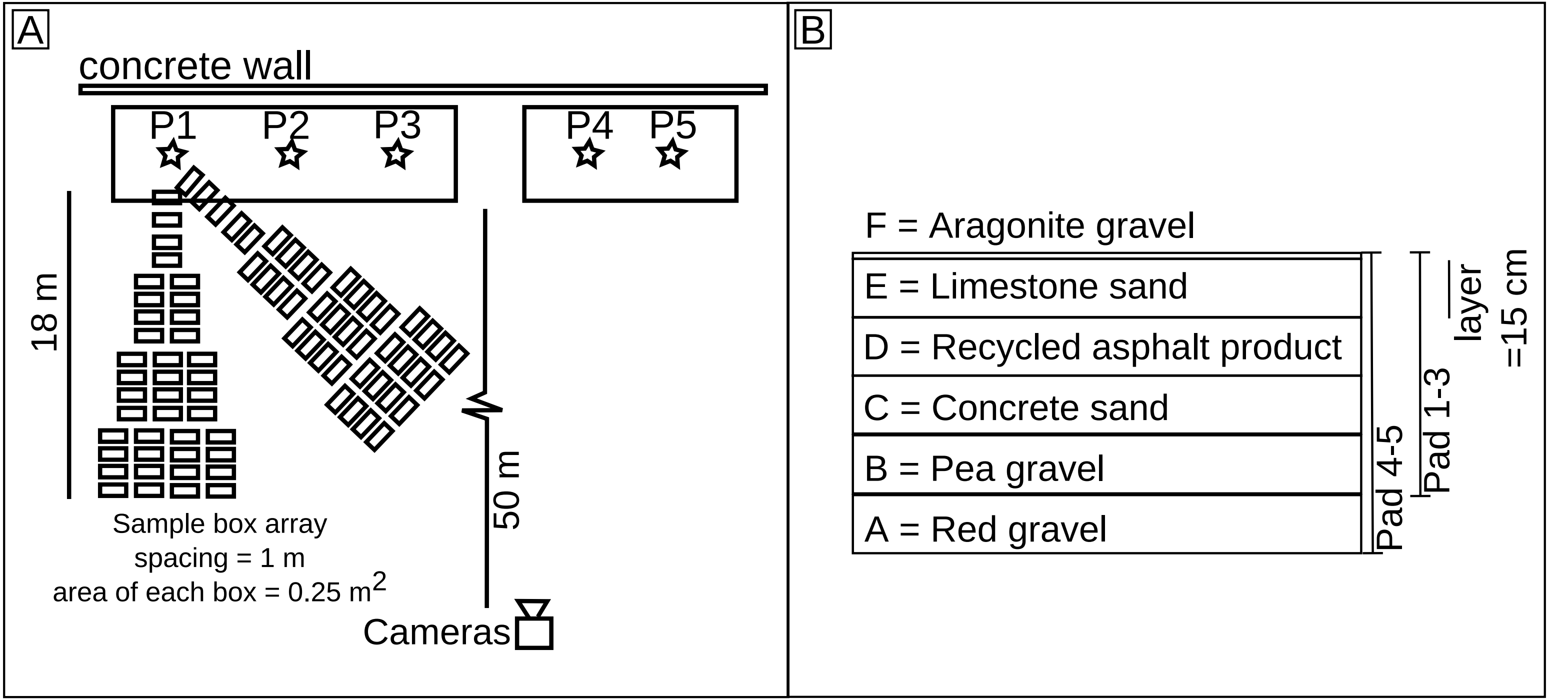
A
concrete wall
P1
P2
P3
P4
P5
18 m
50 m
Sample box array
spacing = 1 m
area of each box = 0.25 m2
Cameras
B
F = Aragonite gravel
E = Limestone sand
D = Recycled asphalt product
C = Concrete sand
B = Pea gravel
A = Red gravel
Pad 4-5
Pad 1-3
layer =15 cm

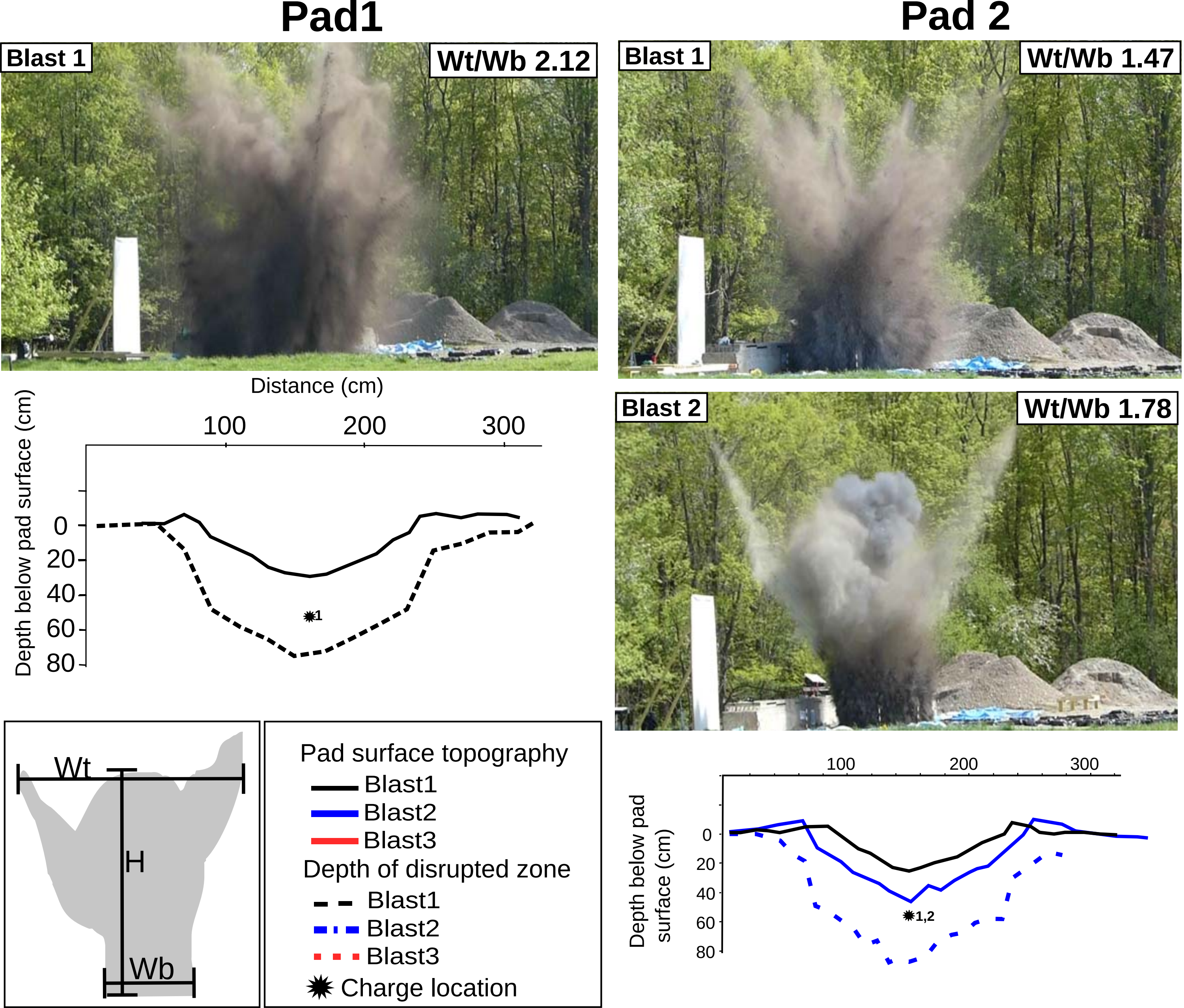
Pad1
Pad 2
Blast 1
Wt/Wb 2.12
Blast 1
Wt/Wb 1.47
Blast 2
Wt/Wb 1.78
Distance (cm)
100
200
300
Depth below pad surface (cm)
0
20
40
60
80
1
100
200
300
Depth below pad surface (cm)
0
20
40
60
80
1,2
Wt
H
Wb
Pad surface topography
Blast1
Blast2
Blast3
Depth of disrupted zone
Blast1
Blast2
Blast3
Charge location


P1B1
P3B1
P4B1
P5B1
P2B1
P3B2
P4B2
P5B2
P2B2
P3B3
P4B3
P5B3

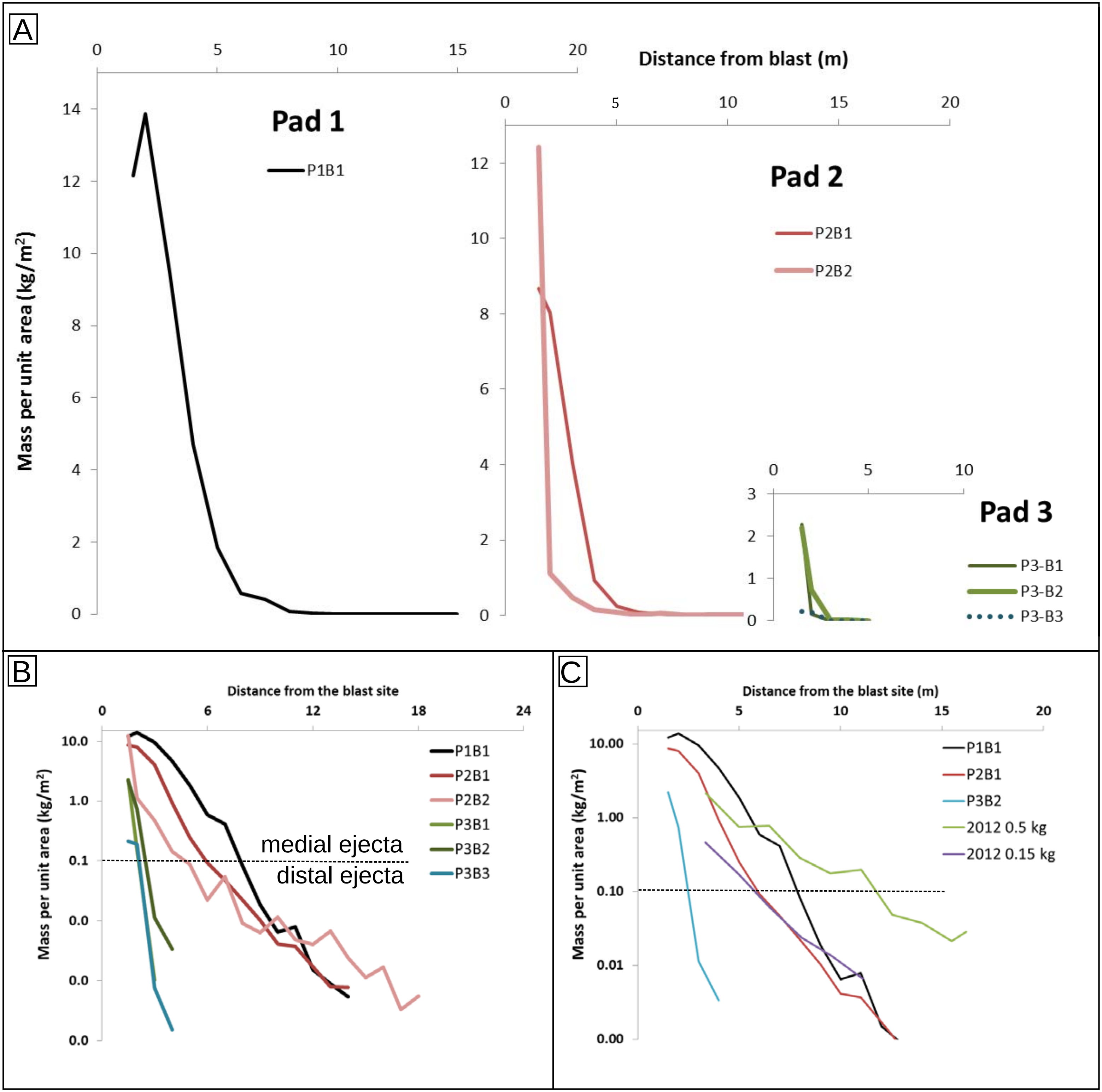

A
Distance from blast (m)
Mass per unit area (kg/m²)
Pad 1
P1B1
Pad 2
P2B1
P2B2
Pad 3
P3-B1
P3-B2
P3-B3
B
Distance from the blast site
Mass per unit area (kg/m²)
10.0
1.0
0.1
0.0
P1B1
P2B1
P2B2
P3B1
P3B2
P3B3
medial ejecta
distal ejecta
C
Distance from the blast site (m)
Mass per unit area (kg/m²)
10.00
1.00
0.10
0.01
0.00
P1B1
P2B1
P3B2
2012 0.5 kg
2012 0.15 kg

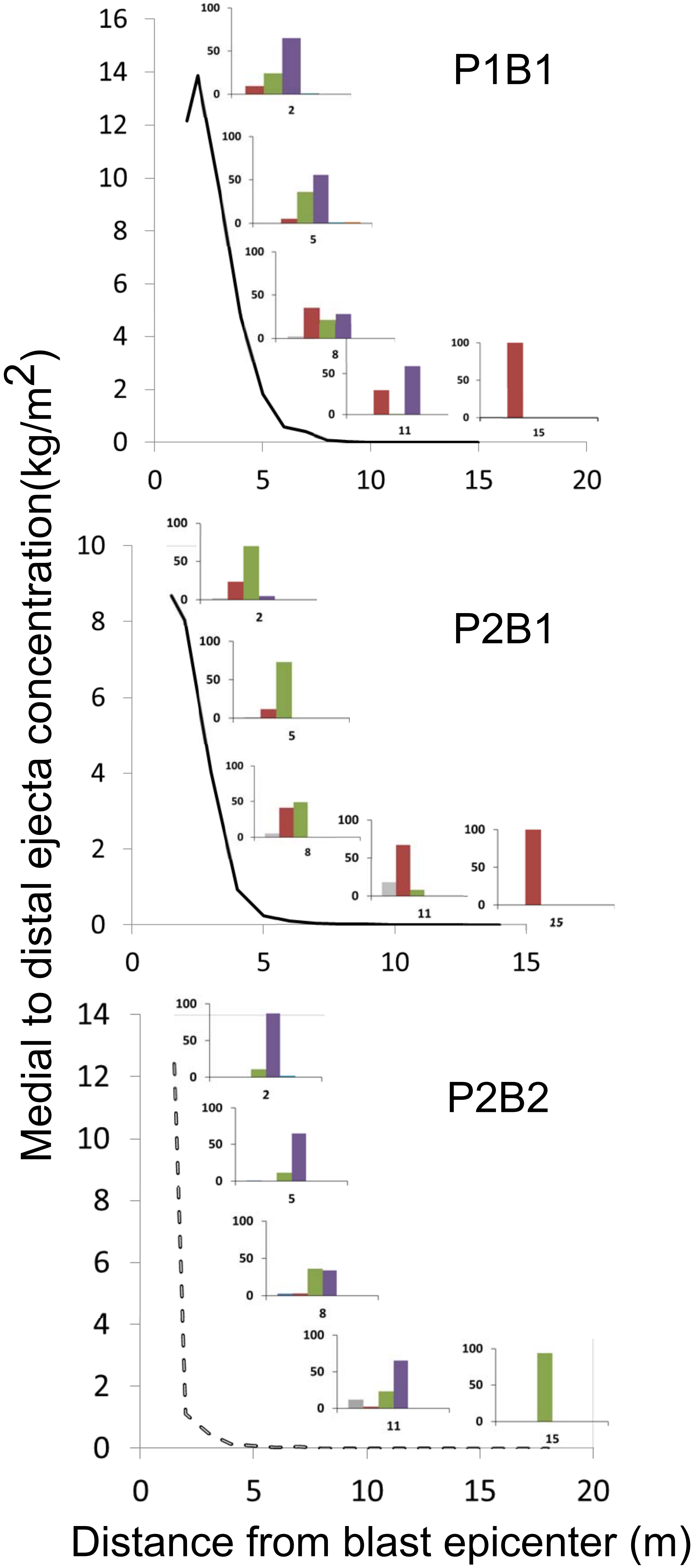
P1B1
16
14
12
10
8
6
4
2
0
0
5
10
15
20
100
50
0
2
5
8
11
15
P2B1
10
8
6
4
2
0
0
5
10
15
P2B2
14
12
10
8
6
4
2
0
0
5
10
15
20
Medial to distal ejecta concentration(kg/m^2)
Distance from blast epicenter (m)

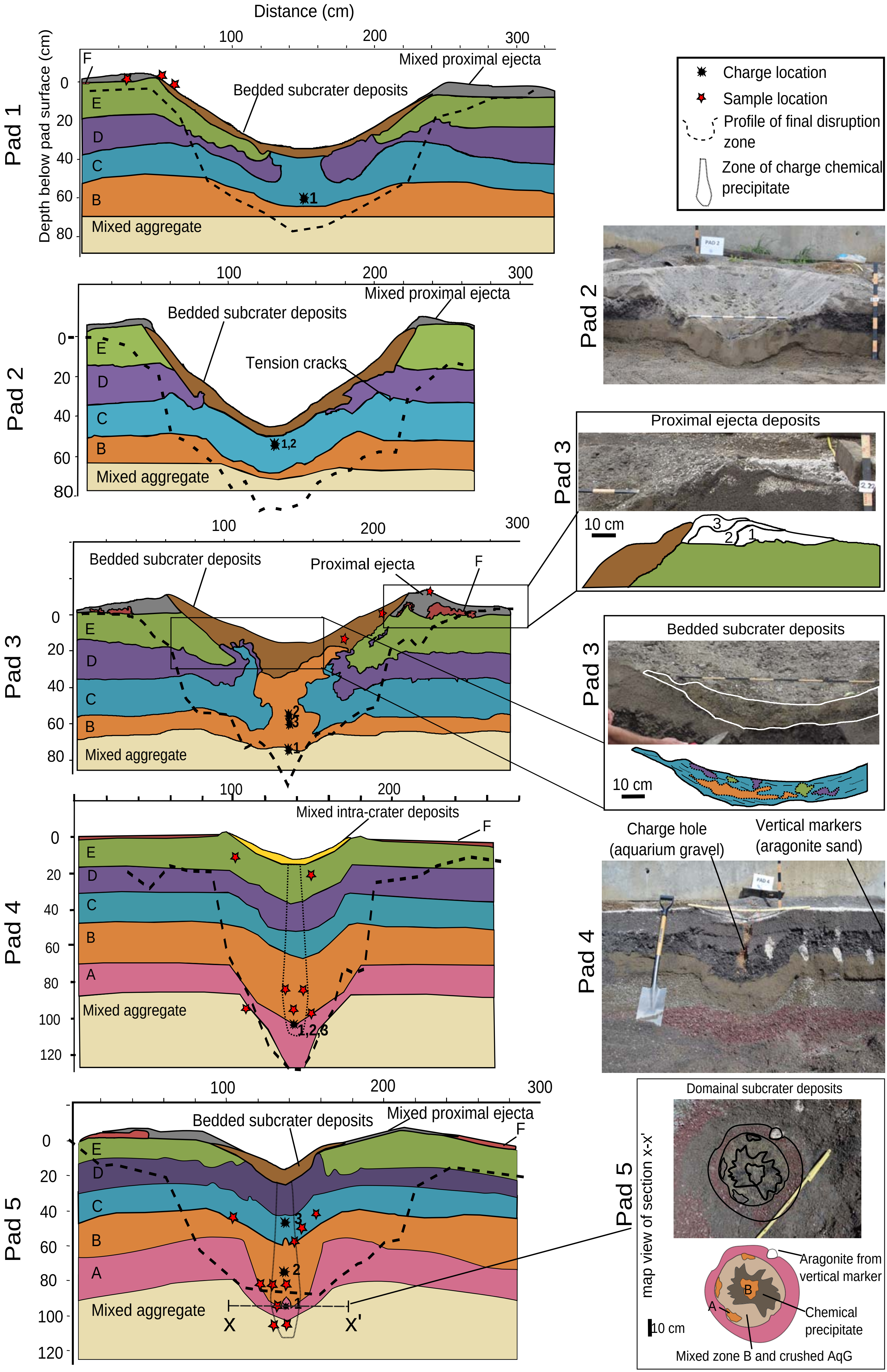
Distance (cm)
100
200
300
Depth below pad surface (cm)
0
20
40
60
80
100
120
Pad 1
F
Mixed proximal ejecta
Bedded subcrater deposits
E
D
C
B
1
Mixed aggregate
Charge location
Sample location
Profile of final disruption zone
Zone of charge chemical precipitate
Pad 2
Tension cracks
1,2
PAD 2
Proximal ejecta deposits
Pad 3
10 cm
3
2
1
Proximal ejecta
2,22
Bedded subcrater deposits
Pad 4
Mixed intra-crater deposits
A
1,2,3
Charge hole (aquarium gravel)
Vertical markers (aragonite sand)
PAD 4
Pad 5
X
X'
Domainal subcrater deposits
map view of section x-x'
Aragonite from vertical marker
Chemical precipitate
Mixed zone B and crushed AqG

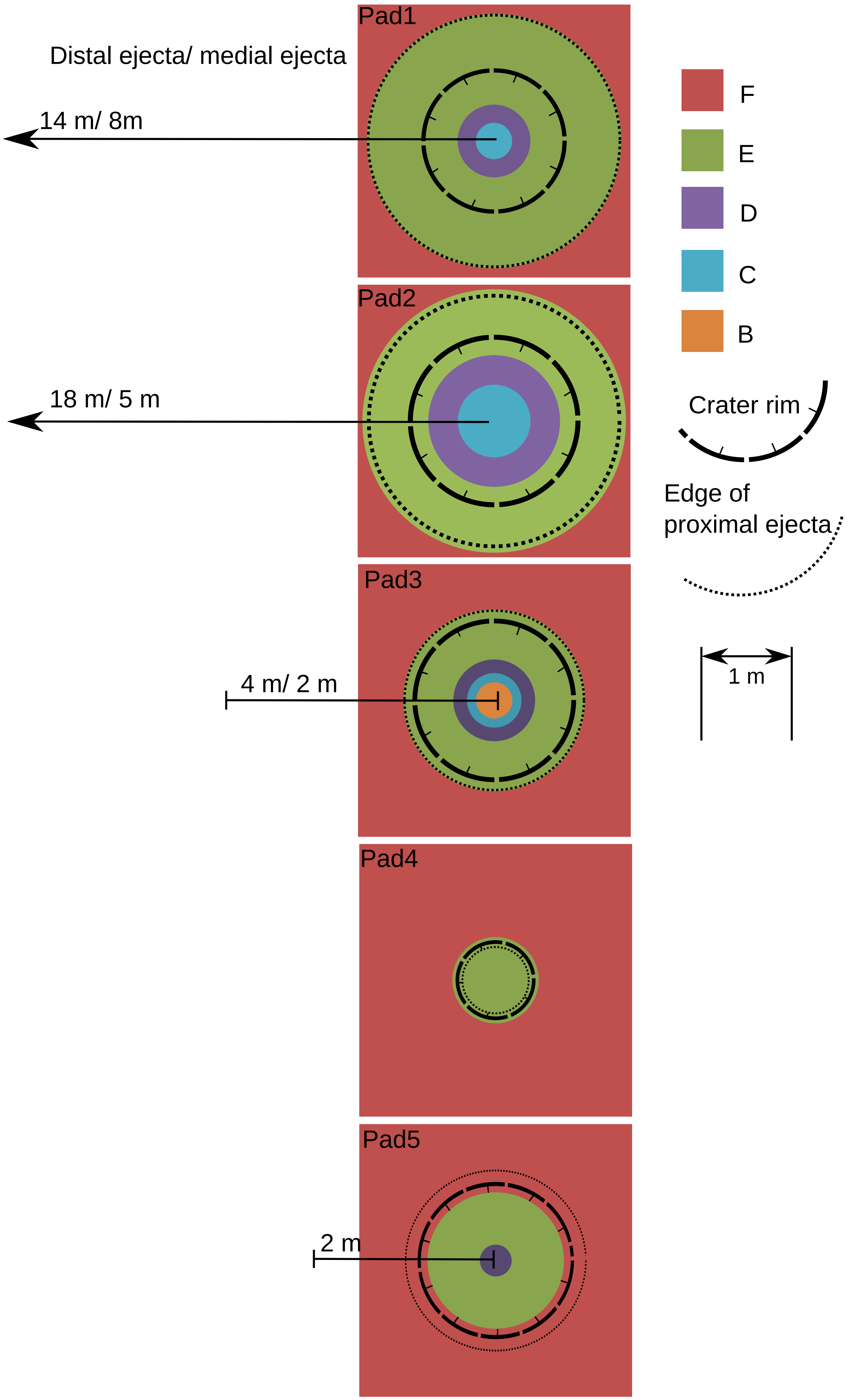
Distal ejecta/ medial ejecta
Pad1
14 m/ 8m
Pad2
18 m/ 5 m
Pad3
4 m/ 2 m
Pad4
Pad5
2 m
F
E
D
C
B
Crater rim
Edge of
proximal ejecta
1 m

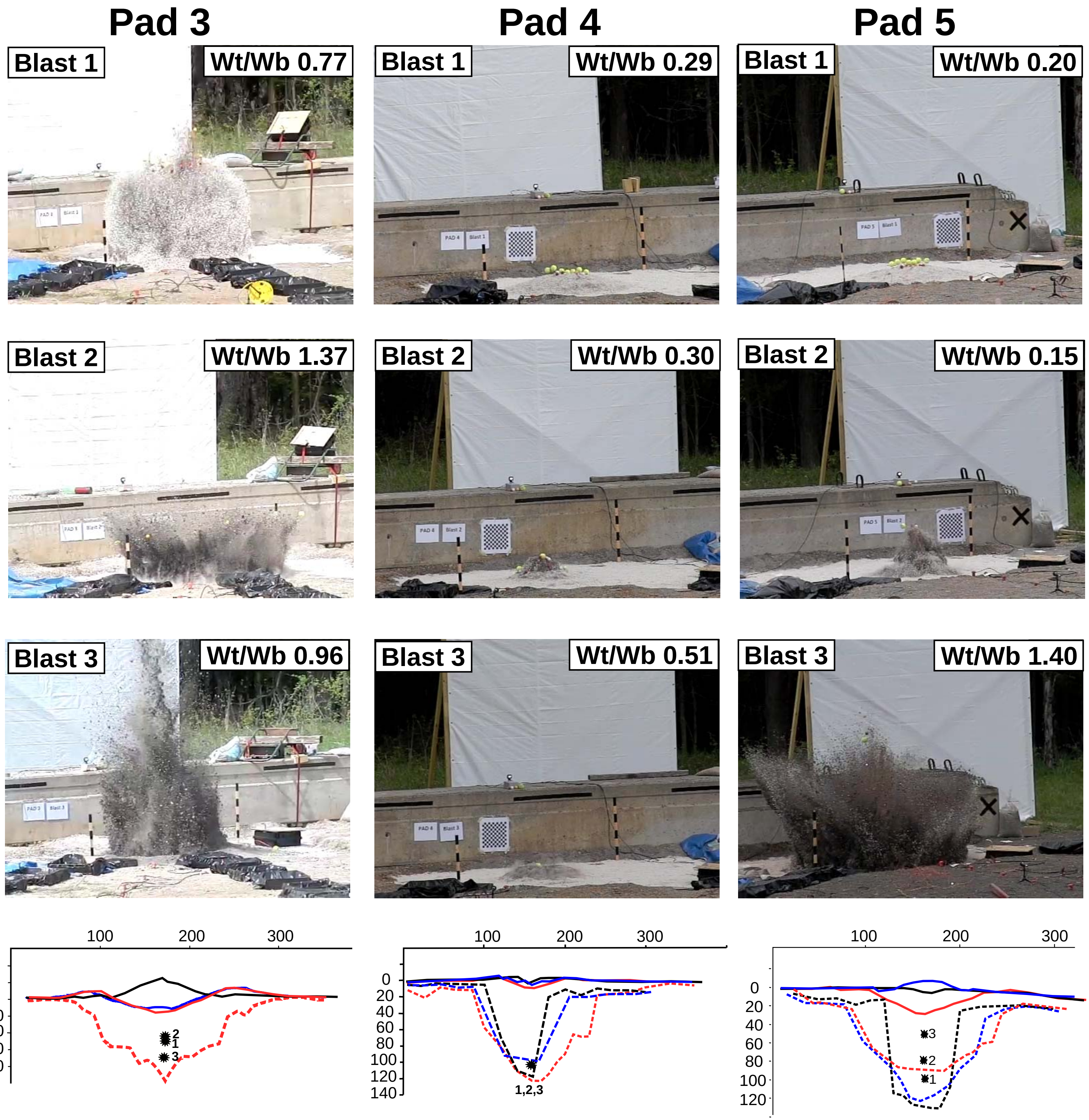
Pad 3
Pad 4
Pad 5
Blast 1
Wt/Wb 0.77
Blast 1
Wt/Wb 0.29
Blast 1
Wt/Wb 0.20
Blast 2
Wt/Wb 1.37
Blast 2
Wt/Wb 0.30
Blast 2
Wt/Wb 0.15
Blast 3
Wt/Wb 0.96
Blast 3
Wt/Wb 0.51
Blast 3
Wt/Wb 1.40
100
200
300
0
20
40
60
80
2
1
3
100
200
300
0
20
40
60
80
100
120
140
1,2,3
100
200
300
0
20
40
60
80
100
120
3
2
1

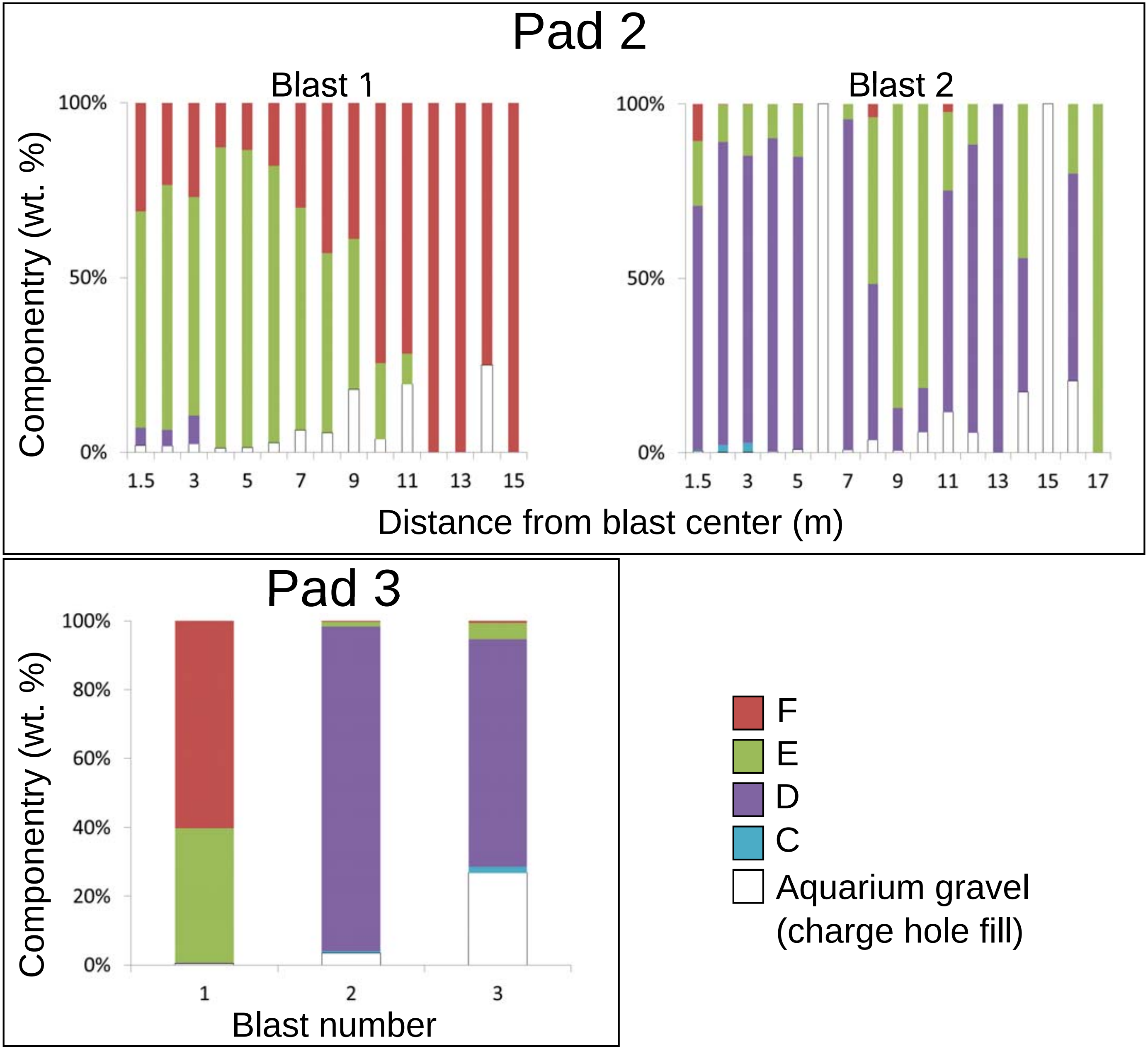
Pad 2
Blast 1
Blast 2
Componentry (wt. %)
100%
50%
0%
1.5
3
5
7
9
11
13
15
17
Distance from blast center (m)
Pad 3
100%
80%
60%
40%
20%
0%
1
2
3
Blast number
F
E
D
C
Aquarium gravel (charge hole fill)

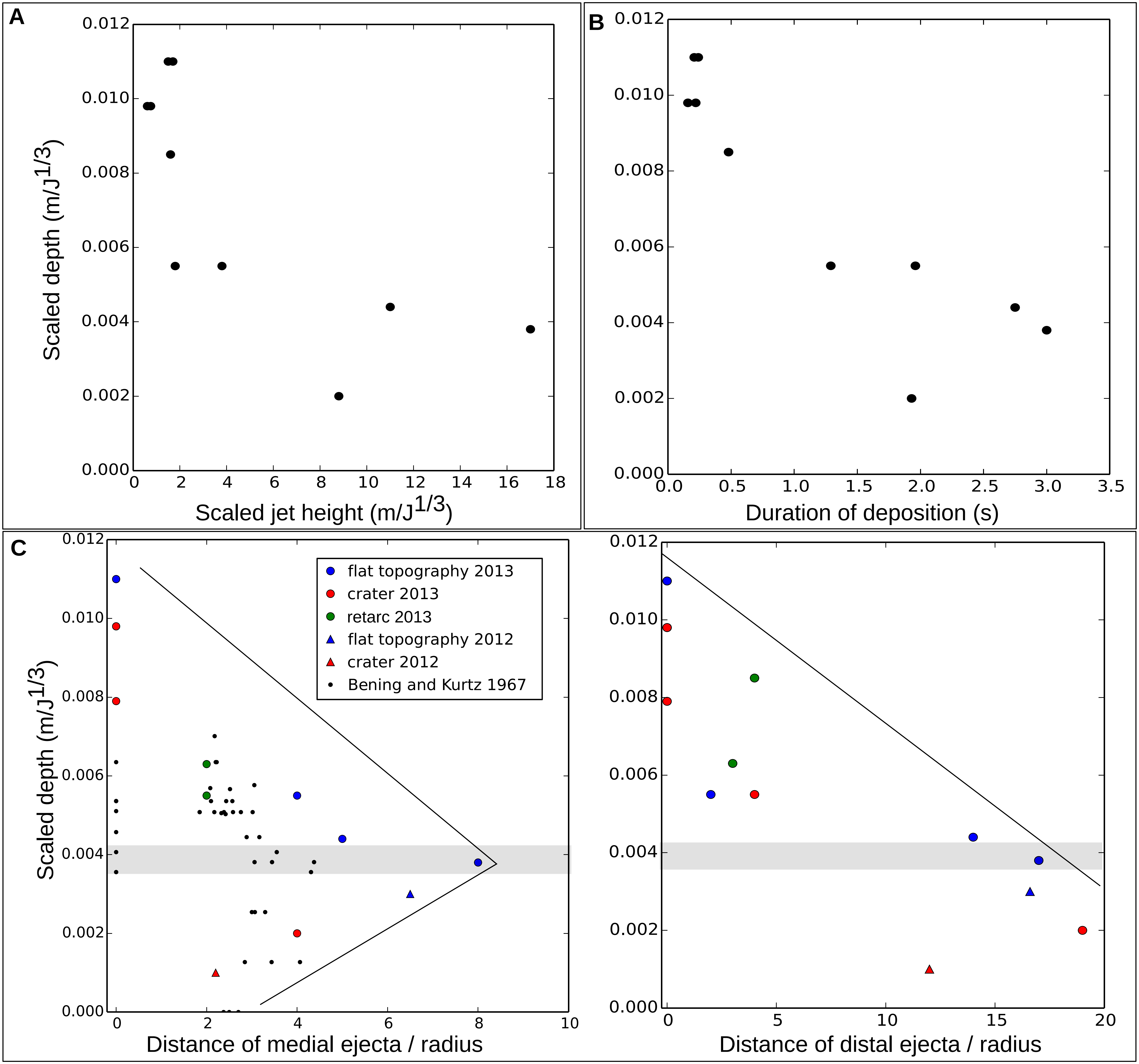
A
Scaled depth ($m/J^{1/3}$)
0.000
0.002
0.004
0.006
0.008
0.010
0.012
0
2
4
6
8
10
12
14
16
18
Scaled jet height ($m/J^{1/3}$)
B
0.000
0.002
0.004
0.006
0.008
0.010
0.012
0.0
0.5
1.0
1.5
2.0
2.5
3.0
3.5
Duration of deposition (s)
C
Scaled depth ($m/J^{1/3}$)
0.000
0.002
0.004
0.006
0.008
0.010
0.012
0
2
4
6
8
10
Distance of medial ejecta / radius
flat topography 2013
crater 2013
retarc 2013
flat topography 2012
crater 2012
Bening and Kurtz 1967
0.000
0.002
0.004
0.006
0.008
0.010
0.012
0
5
10
15
20
Distance of distal ejecta / radius

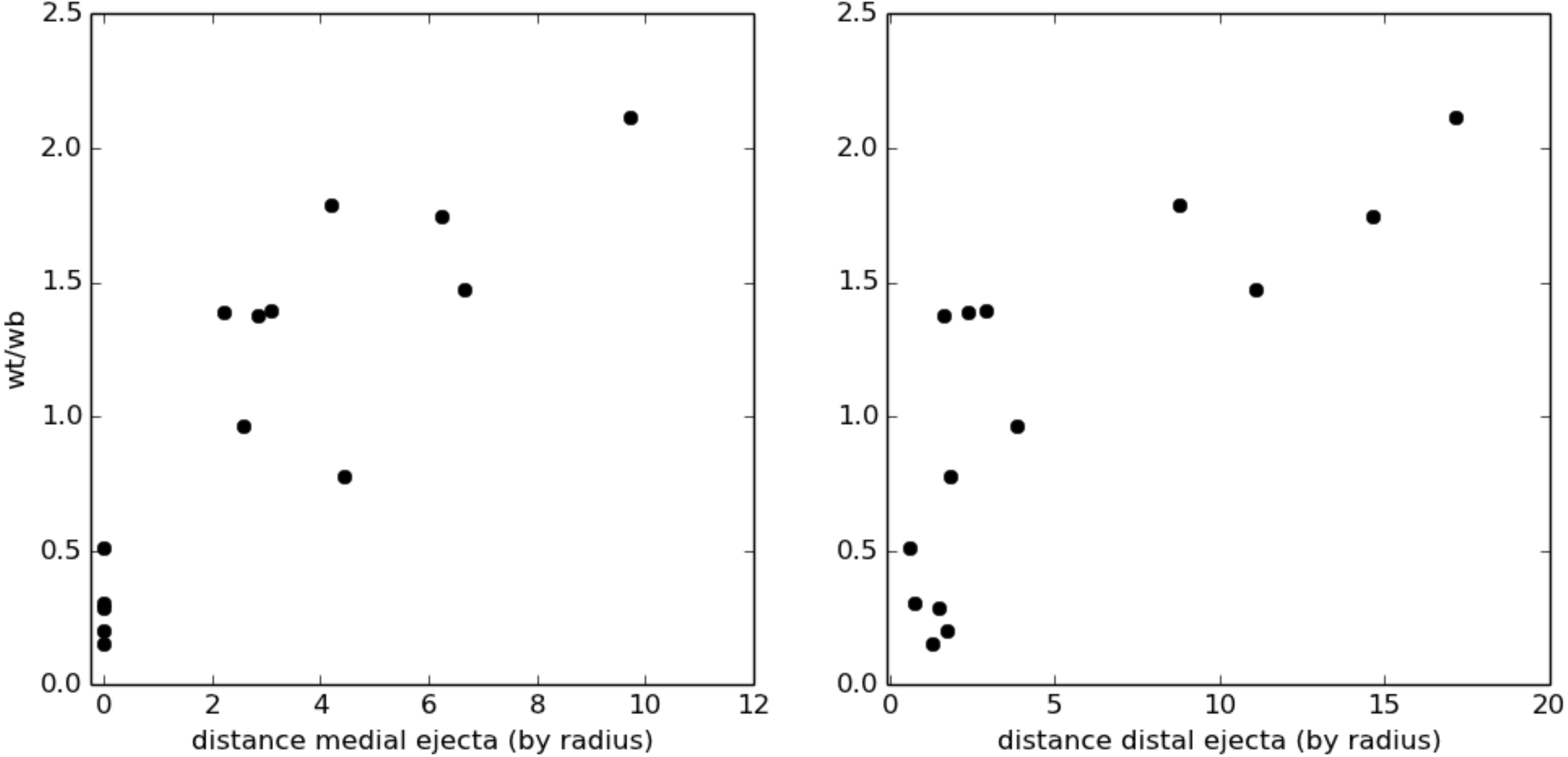
wt/wb
2.5
2.0
1.5
1.0
0.5
0.0
0
2
4
6
8
10
12
distance medial ejecta (by radius)
2.5
2.0
1.5
1.0
0.5
0.0
0
5
10
15
20
distance distal ejecta (by radius)

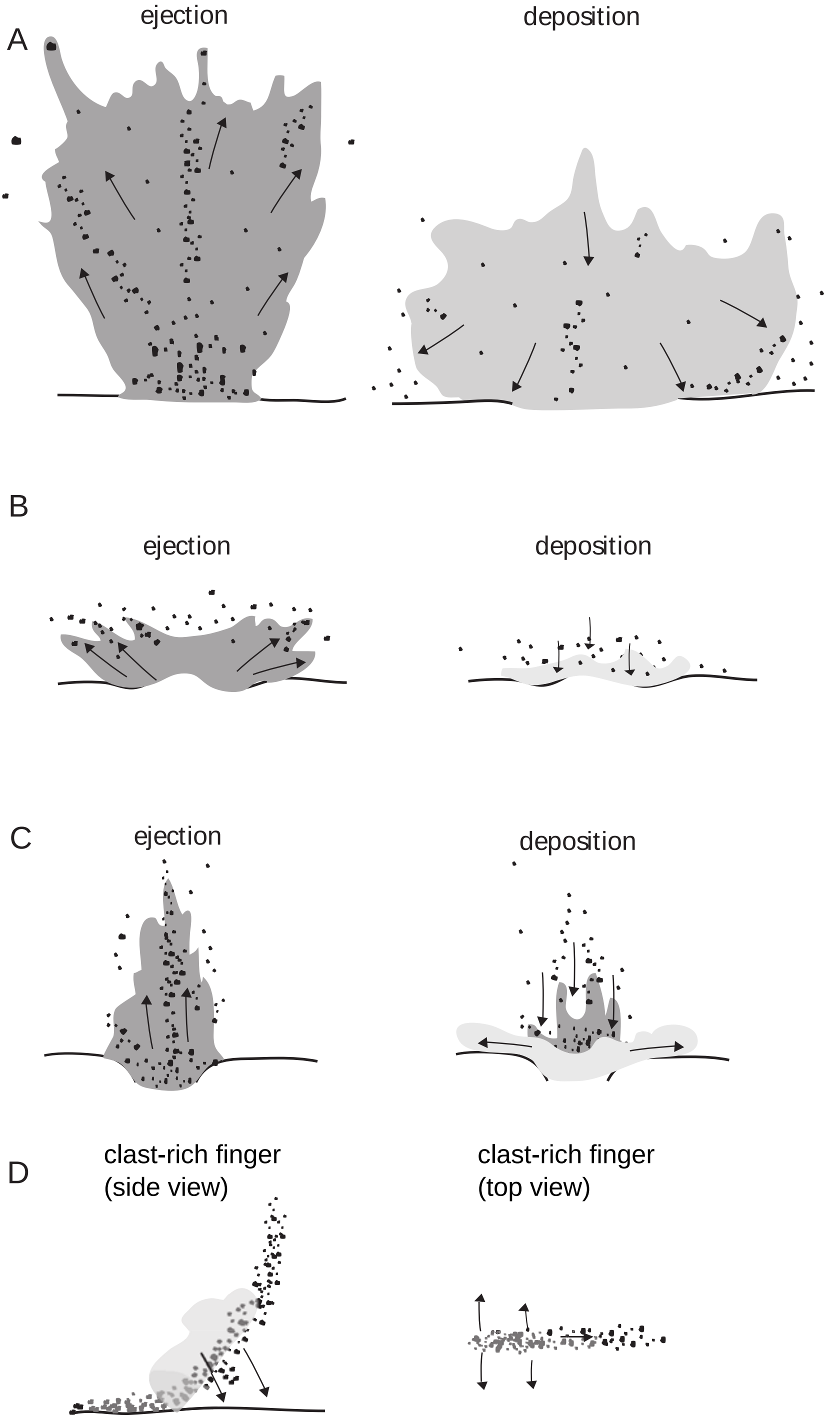
A
ejection
deposition
B
ejection
deposition
C
ejection
deposition
D
clast-rich finger (side view)
clast-rich finger (top view)

Suoana Crater, Miyakejima Japan

Pad 3 excavation this study

2013 Experiments Geshi et al. 2011

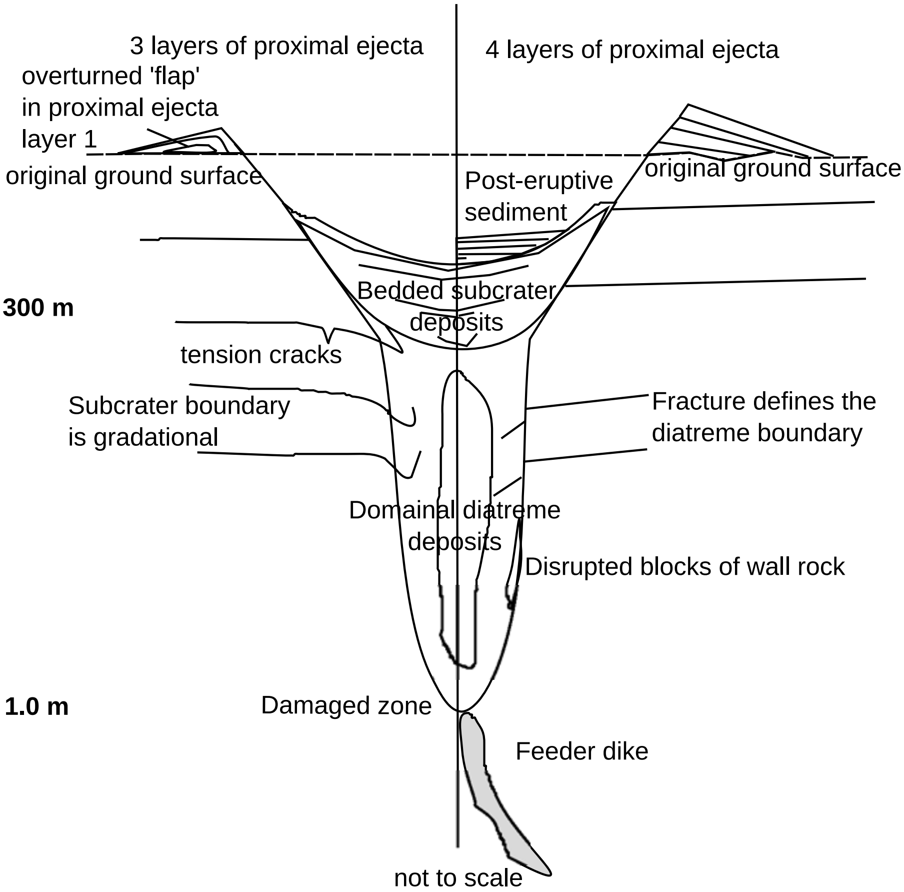

Auxiliary material for

Maar-diatreme geometry and deposits: subsurface blast experiments with variable explosion depth

Graettinger, A.H.[1]; Valentine, G.A.[1]; Sonder, I.[1]; Ross, P.-S.[2], White, J.D.L.[3], Taddeucci, J.[4]

1 Center for Geohazards Studies, 411 Cook Hall, University at Buffalo, Buffalo, NY, 14260, USA

2 Institut national de la recherche scientifique, centre Eau Terre Environnement, 490, Rue de la Couronne, Québec (QC), G1K 9A9, Canada

3 Geology Department, University of Otago, Dunedin, New Zealand

4 Istituto Nazionale di Geofisica e Vulcanologia (INGV), Roma, Italy

Geochemistry, Geophysics and Geosystems

Introduction

These video files (.avi) were collected during the blast experiments at the UB Field Station, NY. The files represent high definition and high speed video of the experiments, representing different pad conditions. Each video has a separate file that have been cut down to size and compressed. The videos are

1 msP1B1.avi High definition video of Pad 1 Blast 1 where a 0.45 charge was detonated at a depth of 0.5 cm (optimal scaled depth) in an undisturbed pad with no topography. Black and white scale bars have increments of 10 cm and horizontal black lines on the concrete wall are 1 m long.

2 msP2B2.avi High definition video of Pad 2 Blast 2 where the charge was detonated beneath an existing crater in a disrupted pad (0.3 kg charge at 26 cm below the crater bottom, low scaled depth). Black and white scale bars have increments of 10 cm and horizontal black lines on the concrete wall are 1 m long.

3 msP3B2.avi High speed video (300 frames per second) of Pad 3 Blast 2 where the charge was detonated beneath a retarc (mound) that was produced by a previous blast (0.15 kg charge at 50 cm below the top of the retarc). Black and white scale bars have increments of 10 cm and horizontal black lines on the concrete wall are 1 m long.

4 msP4B1.avi High speed video (300 frames per second) of Pad 4 Blast 1 where the charge was detonated in an undisturbed pad with no topography, well below the optimal scaled depth (0.15 kg charge at 1 m). Black and white scale bars have increments of 10 cm and horizontal black lines on the concrete wall are 1 m long.

Supplementarymaterial.docx Supplementary table 1 contains granulometric data on the aggregate materials used to create the experimental set up.